Available online at www.sciencedirect.com
SCIENCE DIRECT®
Journal of Sound and Vibration 279 (2005) 417–451
JOURNAL OF SOUND AND VIBRATION
www.elsevier.com/locate/jsvi

Non-linear dynamic analysis of a multi-mesh gear train using multi-term harmonic balance method: sub-harmonic motions

A. Al-shyyab[a], A. Kahraman[b,*]

[a] *The University of Toledo, Toledo, OH 43606, USA*
[b] *Department of Mechanical Engineering, The Ohio State University, Columbus, OH 43210-1107, USA*

Received 7 July 2003; accepted 8 November 2003

Abstract

In this study, a non-linear time-varying dynamic model is used to investigate sub-harmonic and chaotic motions exhibited by a typical multi-mesh gear train. The purely torsional system is formed by three rigid shafts connected to each other by two spur gear pairs. The lumped parameter dynamic model includes both gear backlash clearances and parametric gear mesh stiffness fluctuations. Steady state period-one motions of the same system were studied in another by using a multi-term harmonic balance method in conjunction with discrete Fourier transforms. This study expands the same solution technique for an investigation of sub-harmonic resonances of the forced response. The accuracy of the predictions is demonstrated by comparing them to the direct numerical integration results. Effect of several system parameters such as alternating mesh stiffness amplitudes, gear mesh damping and static torque transmitted on sub-harmonic motions are described. It is shown that stable sub-harmonic motions mostly in the form of softening type resonances dictate the frequency ranges in which the period-one motions are unstable due to parametric excitations. Other non-linear phenomena including long sub-harmonic motions and period-doubling bifurcations leading to chaotic behavior are also predicted.

1. Introduction

Dynamic behavior of gear systems has been one of the main topics in power transmission research. Both fatigue life and noise behavior of a gear set is influenced by its dynamic behavior. Since gear mesh and support bearing forces increase under typical dynamic operating conditions, dynamic forces transmitted to the housing and other structures are also increased, resulting in

*Corresponding author. Tel.: +1-614-292-4678; fax: +1-614-292-3603.
E-mail address: kahraman.1@osu.edu (A. Kahraman).

0022-460X/$ - see front matter © 2003 Elsevier Ltd. All rights reserved.
doi:10.1016/j.jsv.2003.11.029

excessive noise levels attributable to the gears. Likewise, dynamic loads at the gear mesh cause elevated tooth root and contact stresses, leading to shorter tooth bending and pitting fatigue lives.

The gear system that will be studied in this paper, as shown in Fig. 1, is a multi-mesh gear train that is formed by three shafts and two gear pairs. As one of the most common configurations used in automotive, aerospace, marine and industrial power trains, this arrangement can be found in passenger car automatic, manual and continuously variable transmissions, commercial industrial gearboxes and helicopter drive trains. A number of models were proposed in the past to describe the dynamic behavior of this system. Most of these models were linear time-invariant type as the gear backlash and mesh stiffness fluctuations were both ignored [1–13]. Such simplifications allowed larger number of degrees of freedom to be included in the models since eigenvalue and modal summation formulations were suitable. Shaft and bearing flexibilities and combined transverse-torsional motions of gears were all included in these models to study larger-scale gear–shaft-bearing systems. In some cases, even the case housing flexibilities were included in the form of a case stiffness matrix [13]. While these models offered guidelines towards the design of gear systems with favorable shaft and bearing arrangements, they brought limited insight to the behavior at the gear mesh. Meanwhile, the recent experimental data [14–16] indicated that tooth separations are observed commonly, suggesting that the models must include gear backlash non-linearity. In addition, the mesh stiffness fluctuations were found to be one of the main excitations originating from the spur gear mesh, and hence, they must be included in a gear dynamics model as well [17].

Another group of models included the mesh stiffness fluctuations in the form of a parametric excitation while still assuming no tooth separations. Papers by Benton and Seireg [18,19], Mollers [20], Nakada and Utagawa [21], and most recently, Lin and Parker [22] focused on the instabilities caused by parametric excitations. These studies presented stability maps that define the ranges of unstable motions as a function of gear mesh damping and mesh stiffness excitation amplitudes. Sinusoidal and rectangular functions were considered as extreme cases of mesh stiffness

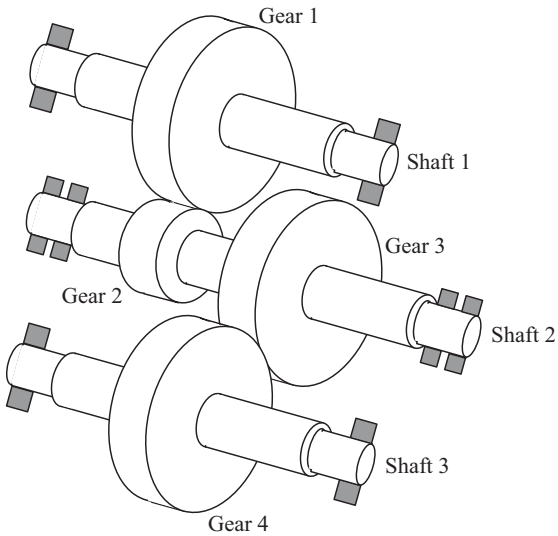

Fig. 1. The multi-mesh gear train considered in this study.

variations. It was predicted that gear systems could exhibit both primary and sub-harmonic resonances resulting in regions of unstable motions with very large amplitudes.

Experimental studies by Gregory et al. [23], Kahraman and Blankenship [14,16], Umezawa et al. [24] indicate that unstable regions predicted by linear time-varying models are dictated by bounded sub-harmonic motions. As the vibration amplitudes get larger in these regions, tooth separations are initiated. This results in a softening type response (bending to the left) that is formed by period-n (nT) sub-harmonic motions ($n \geqslant 2$). Models of Kahraman and Blankenship [16], and Kahraman and Singh [25] included both the gear backlash and mesh stiffness fluctuations, and exhibited this behavior for a single gear pair. Most recently, Al-shyyab and Kahraman [26] proposed a non-linear time-varying dynamic model of the system shown in Fig. 1. The system was reduced to a two-degree-of-freedom definite model by using the relative gear mesh displacements as the co-ordinates. Dimensionless equations of motion were solved for the steady state period-1 ($1T$) response by using a multi-term harmonic balance method (HBM) in conjunction with discrete Fourier transforms and a parametric continuation scheme. The HBM solutions were shown to be accurate by comparing them to direct numerical integration (NI) solutions. Floquet theory was applied to determine the stability of the steady state HBM solutions. An example gear train was used to investigate the influence of key system parameters including alternating mesh stiffness amplitudes, gear mesh damping, static torque transmitted and the gear mesh frequency ratio.

1.1. Scope and objectives

In this study, the non-linear time-varying dynamic model of the gear system shown in Fig. 1, as proposed in Ref. [26], will be used to study sub-harmonic and chaotic motions. Both the gear backlash clearance and the parametric gear mesh stiffness fluctuations will be included in the model. Steady state nT ($n \geqslant 2$) motions of the same system will be determined by using a multi-term HBM in conjunction with discrete Fourier transforms. Sub-harmonic resonances in the instability ranges will be predicted. Accuracy of the predictions will be demonstrated by comparing them to the NI results. The effect of several system parameters such as alternating mesh stiffness amplitudes, gear mesh damping and static torque transmitted on sub-harmonic motions will also be investigated. Other non-linear phenomena including long sub-harmonic motions, period doubling bifurcations and chaotic behavior will also be demonstrated.

2. Dynamic model and equations of motion

Sub-harmonic and chaotic motions exhibited by the system shown in Fig. 1 is the main focus of this study. The system consists of two separate gear meshes. Four gears mounted on three shafts form this gear train. The torsional dynamic model shown in Fig. 2 was proposed in Ref. [26]. We refer to this previous paper for the details of the dynamic model, assumptions employed and non-dimensionalization of the equations of motion. In this study, only the details of the model formulation that are relevant to sub-harmonic motions will be included.

In Fig. 2, each gear of polar mass moment of inertia I_i and base radius r_i is allowed to vibrate in torsional direction by $\bar{\theta}_i$ ($i = 1$–4). Here, $\bar{\theta}_i$ represents the vibrations of gear i about its nominal

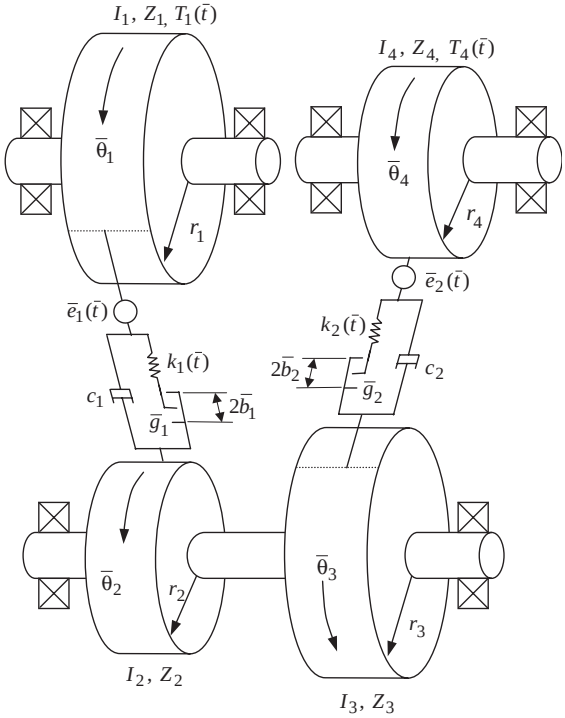

Fig. 2. Dynamic model of the physical system shown in Fig. 1.

rigid body rotation $\Omega_i \bar{t}$ where Ω_i is rotational speed in radians per second and $\bar{t}$ is real time in seconds. Functions $k_1(\bar{t})$ and $k_2(\bar{t})$ represent gear mesh flexibilities of the first and second gear meshes, respectively. The gear mesh damping values are denoted by c_1 and c_2. These stiffness and damping elements were applied at respective gear meshes in the direction of the gear mesh line of action. Displacement excitations $e_1(\bar{t})$ and $e_2(\bar{t})$ are connected in series to the stiffness and damping elements as shown in Fig. 2. Gear backlash non-linearity is modelled as piecewise linear "dead-zone" type clearance functions $\bar{g}_1$ and $\bar{g}_2$ of amounts $2\bar{b}_1$ and $2\bar{b}_2$, respectively, and applied to the displacement terms only. Here, neither the backlash functions nor the time-varying effects are applied to the gear mesh damping. This is partly because of the fact that the damping coefficients c_1 and c_2 in this model represent an array of different damping mechanisms including gear mesh, windage, lubrication and bearings. In addition, it was also reported earlier that the predictions of single gear pairs models with constant damping agree well with experimental data [15,16]. Therefore, linear time-invariant viscous damping values are considered here.

It is assumed in Fig. 2 that the torsional shaft flexibilities are negligible. However, this assumption might not be valid for a system having a relatively long shaft segment between gears 2 and 3. In such cases, $\bar{\theta}_2(\bar{t}) \neq \bar{\theta}_3(\bar{t})$ and a torsional spring must be defined between these two gears increasing the degrees of freedom to three. Likewise, one could include the inertias of the input and output as well that would introduce two additional co-ordinates. In order to keep the model formulations at a manageable level, only the limiting case of rigid shafts is considered here by

letting $\bar{\theta}_2(\bar{t}) = \bar{\theta}_3(\bar{t})$ and $I_{23} = I_2 + I_3$, and using relative gear mesh displacements

$$\bar{p}_1(\bar{t}) = r_1\bar{\theta}_1(\bar{t}) + r_2\bar{\theta}_2(\bar{t}) + \bar{e}_1(\bar{t}), \qquad \bar{p}_2(\bar{t}) = r_3\bar{\theta}_2(\bar{t}) + r_4\bar{\theta}_4(\bar{t}) + \bar{e}_2(\bar{t}), \tag{1a, b}$$

as the co-ordinates, the equations of motion can be written as [26]

$$\ddot{\bar{p}}_1(\bar{t}) + c_1\left[\frac{r_1^2}{I_1} + \frac{r_2^2}{I_{23}}\right]\dot{\bar{p}}_1(\bar{t}) + c_2\left[\frac{r_2 r_3}{I_{23}}\right]\dot{\bar{p}}_2(\bar{t}) + k_1(\bar{t})\left[\frac{r_1^2}{I_1} + \frac{r_2^2}{I_{23}}\right]\bar{g}_1(\bar{t}) + k_2(\bar{t})\left[\frac{r_2 r_3}{I_{23}}\right]\bar{g}_2(\bar{t}) = \frac{r_1}{I_1}\bar{T}_1(\bar{t}) + \ddot{\bar{e}}_1(\bar{t}), \tag{2a}$$

$$\ddot{\bar{p}}_2(\bar{t}) + c_1\left[\frac{r_2 r_3}{I_{23}}\right]\dot{\bar{p}}_1(\bar{t}) + c_2\left[\frac{r_3^2}{I_{23}} + \frac{r_4^2}{I_4}\right]\dot{\bar{p}}_2(\bar{t}) + \left[\frac{r_2 r_3}{I_{23}}\right]k_1(\bar{t})\bar{g}_1(\bar{t}) + k_2(\bar{t})\left[\frac{r_3^2}{I_{23}} + \frac{r_4^2}{I_4}\right]\bar{g}_2(\bar{t}) = \frac{r_4}{I_4}\bar{T}_4(\bar{t}) + \ddot{\bar{e}}_2(\bar{t}). \tag{2b}$$

Here $\bar{g}_1$ and $\bar{g}_2$ are gear backlash functions defined as

$$\bar{g}_1 = \begin{cases} [r_1\bar{\theta}_1(\bar{t}) + r_2\bar{\theta}_2(\bar{t}) + \bar{e}_1(\bar{t})] - \bar{b}_1, & [r_1\bar{\theta}_1(\bar{t}) + r_2\bar{\theta}_2(\bar{t}) + \bar{e}_1(\bar{t})] > \bar{b}_1, \\ 0, & |r_1\bar{\theta}_1(\bar{t}) + r_2\bar{\theta}_2(\bar{t}) + \bar{e}_1(\bar{t})| \leqslant \bar{b}_1, \\ [r_1\bar{\theta}_1(\bar{t}) + r_2\bar{\theta}_2(\bar{t}) + \bar{e}_1(\bar{t})] + \bar{b}_1, & [r_1\bar{\theta}_1(\bar{t}) + r_2\bar{\theta}_2(\bar{t}) + \bar{e}_1(\bar{t})] < -\bar{b}_1, \end{cases} \tag{3a}$$

$$\bar{g}_2 = \begin{cases} [r_3\bar{\theta}_2(\bar{t}) + r_4\bar{\theta}_4(\bar{t}) + \bar{e}_2(\bar{t})] - \bar{b}_2, & [r_3\bar{\theta}_2(\bar{t}) + r_4\bar{\theta}_4(\bar{t}) + \bar{e}_2(\bar{t})] > \bar{b}_2, \\ 0, & |r_3\bar{\theta}_2(\bar{t}) + r_4\bar{\theta}_4(\bar{t}) + \bar{e}_2(\bar{t})| \leqslant \bar{b}_2, \\ [r_3\bar{\theta}_2(\bar{t}) + r_4\bar{\theta}_4(\bar{t}) + \bar{e}_2(\bar{t})] + \bar{b}_2, & [r_3\bar{\theta}_2(\bar{t}) + r_4\bar{\theta}_4(\bar{t}) + \bar{e}_2(\bar{t})] < -\bar{b}_2. \end{cases} \tag{3b}$$

Dimensionless equations of motion are obtained by defining

$$m_1 = \frac{I_1 I_{23}}{r_1^2 I_{23} + I_1 r_2^2}, \qquad m_2 = \frac{I_{23}}{r_2 r_3}, \qquad m_3 = \frac{I_4 I_{23}}{r_4^2 I_{23} + I_4 r_3^2}, \tag{4a–c}$$

$$\kappa_1(\bar{t}) = \frac{k_1(\bar{t})}{k_{1m}}, \qquad \kappa_2(\bar{t}) = \frac{k_2(\bar{t})}{k_{2m}}, \tag{4d, e}$$

$$\bar{\omega}_{11}^2 = \frac{k_{1m}}{m_1}, \qquad \bar{\omega}_{12}^2 = \frac{k_{2m}}{m_2}, \qquad \bar{\omega}_{21}^2 = \frac{k_{1m}}{m_2}, \qquad \bar{\omega}_{22}^2 = \frac{k_{2m}}{m_3}, \tag{4f–i}$$

$$\zeta_{11} = \frac{c_1}{2m_1\bar{\omega}_{11}}, \qquad \zeta_{12} = \frac{c_2}{2m_2\bar{\omega}_{12}}, \qquad \zeta_{21} = \frac{c_1}{2m_2\bar{\omega}_{21}}, \qquad \zeta_{22} = \frac{c_2}{2m_3\bar{\omega}_{22}}, \tag{4j–m}$$

where k_{1m} and k_{2m} are the mean components of $k_1(t)$ and $k_2(t)$, respectively. Considering a dimensionless time $t = \bar{t}\omega_c$ where ω_c is the characteristic frequency, and then letting $\omega_{ij} = \bar{\omega}_{ij}/\omega_c$ $(i,j = 1,2)$, $p_i(\bar{t}) = \bar{p}_i(\bar{t})/b_c$, $e_i(\bar{t}) = \bar{e}_i(\bar{t})/b_c$ and $b_i = \bar{b}_i/b_c$ $(i = 1,2)$, where b_c is a characteristic length, dimensionless equations of motion are obtained as [26]

$$\begin{Bmatrix} \ddot{p}_1(t) \\ \ddot{p}_2(t) \end{Bmatrix} + 2\begin{bmatrix} \zeta_{11}\omega_{11} & \zeta_{12}\omega_{12} \\ \zeta_{21}\omega_{21} & \zeta_{22}\omega_{22} \end{bmatrix}\begin{Bmatrix} \dot{p}_1(t) \\ \dot{p}_2(t) \end{Bmatrix} + \begin{bmatrix} \omega_{11}^2\kappa_1(t) & \omega_{12}^2\kappa_2(t) \\ \omega_{21}^2\kappa_1(t) & \omega_{22}^2\kappa_2(t) \end{bmatrix}\begin{Bmatrix} g_1(t) \\ g_2(t) \end{Bmatrix} = \begin{Bmatrix} f_1(t) \\ f_2(t) \end{Bmatrix}, \tag{5a}$$

where

$$g_i(t) = \begin{cases} p_i(t) - b_i, & p_i(t) > b_i, \\ 0, & |p_i(t)| \leqslant b_i, \\ p_i(t) + b_i, & p_i(t) < -b_i, \end{cases} \qquad i = 1, 2, \tag{5b}$$

$$f_1(t) = \frac{r_1 \bar{T}_1(t)}{I_1 \omega_c^2 b_c} + \ddot{e}_1(t), \qquad f_2(t) = \frac{r_4 \bar{T}_4(t)}{I_4 \omega_c^2 b_c} + \ddot{e}_2(t). \tag{5c, d}$$

3. Multi-term harmonic balance solution for sub-harmonic motions

The procedure that was used earlier [26] for solution of period-one motions is expanded here to obtain nT sub-harmonic motions ($n \geqslant 2$). In Fourier series form, periodic functions $\kappa_i(t)$ and $f_i(t)$ are written as

$$\kappa_1(t) = 1 + \sum_{h=1}^{K} [\kappa_{2h}^{(1)} \cos(h\Lambda t) + \kappa_{2h+1}^{(1)} \sin(h\Lambda t)], \tag{6a}$$

$$\kappa_2(t) = 1 + \sum_{h=1}^{K} [\kappa_{2h}^{(2)} \cos(hn\Lambda t) + \kappa_{2h+1}^{(2)} \sin(hn\Lambda t)], \tag{6b}$$

$$f_1(t) = f_1^{(1)} + \sum_{\ell=1}^{L} [f_{2\ell}^{(1)} \cos(\ell\Lambda t) + f_{2\ell+1}^{(1)} \sin(\ell\Lambda t)], \tag{6c}$$

$$f_2(t) = f_1^{(2)} + \sum_{\ell=1}^{L} [f_{2\ell}^{(2)} \cos(\ell\Lambda t) + f_{2\ell+1}^{(2)} \sin(\ell\Lambda t)]. \tag{6d}$$

Here, $\Lambda_1 = \Lambda$ and $\Lambda_2 = n\Lambda$ are the fundamental (gear mesh) frequencies of the stiffness of the first and second gear meshes, respectively, where $\Lambda = Z_1\Omega_1/\omega_c$ is the dimensionless gear mesh frequency (Z_1 is the number of teeth of gear 1), and the multiplier n can be any real number as it defines the ratio of the number of teeth of gears 2 and 3 in Fig. 1, $n = Z_2/Z_3$.

One can assume ηT sub-harmonic solutions, $p_1(t)$ and $p_2(t)$, again written in Fourier series form as

$$p_1(t) = u_1^{(1)} + \sum_{r=1}^{R} \left[u_{2r}^{(1)} \cos\left(\frac{r\Lambda t}{\eta}\right) + u_{2r+1}^{(1)} \sin\left(\frac{r\Lambda t}{\eta}\right) \right], \tag{7a}$$

$$p_2(t) = u_1^{(2)} + \sum_{r=1}^{R} \left[u_{2r}^{(2)} \cos\left(\frac{rn\Lambda t}{\eta}\right) + u_{2r+1}^{(2)} \sin\left(\frac{rn\Lambda t}{\eta}\right) \right]. \tag{7b}$$

Here $u_1^{(1)}, u_{2r}^{(1)}, u_{2r+1}^{(1)}, u_1^{(2)}, u_{2r}^{(2)}, u_{2r+1}^{(2)}$ ($r \in [1, R]$) are unknown coefficients of the assumed solution and η is a sub-harmonic index, introduced to facilitate sub-harmonic solutions. For a harmonic balance to hold in Eq. (5a), the non-linear functions $g_1(t)$ and $g_2(t)$ are required to be periodic as

well at the same harmonic orders as the assumed solutions:

$$g_1(t) = v_1^{(1)} + \sum_{r=1}^{R} \left[v_{2r}^{(1)} \cos\left(\frac{r\Lambda}{\eta} t\right) + v_{2r+1}^{(1)} \sin\left(\frac{r\Lambda}{\eta} t\right) \right], \tag{8a}$$

$$g_2(t) = v_1^{(2)} + \sum_{r=1}^{R} \left[v_{2r}^{(2)} \cos\left(\frac{rn\Lambda}{\eta} t\right) + v_{2r+1}^{(2)} \sin\left(\frac{rn\Lambda}{\eta} t\right) \right], \tag{8b}$$

where the unknown coefficients $v_1^{(i)}$, $v_{2r}^{(i)}$ and $v_{2r+1}^{(i)}$ ($r \in [1, R]$ and $i = 1, 2$), also known as describing functions, must be determined before the unknown response parameters can be found. Given $\theta = \Lambda t/\eta$, a set of $(4R + 3)$ non-linear algebraic equations are obtained by substituting Eqs. (6)–(8) into Eq. (5a), neglecting higher order terms, and equating the coefficients of like harmonics. This set of algebraic equations is written in vector form as

$$\mathbf{S}(\mathbf{U}, \mathbf{v}) = \mathbf{0}. \tag{9}$$

Here $\mathbf{U} = [u_1^{(1)}, u_2^{(1)}, \ldots, u_{2R}^{(1)}, u_{2R+1}^{(1)}, u_1^{(2)}, u_2^{(2)}, \ldots, u_{2R}^{(2)}, u_{2R+1}^{(2)}, u_{4R+3}]^{\mathrm{T}}$, where $u_{4R+3} = \Lambda$, and $\mathbf{S}$ both have dimension $(4R + 3)$, and the elements of $\mathbf{S}$ are given as ($r \in [1, R]$).

$$\begin{aligned} S_1^{(1)} = {} & \omega_{11}^2 \left[v_1^{(1)} + \frac{1}{2} \sum_{i=1}^{R} (v_{2i\eta}^{(1)} \kappa_{2i}^{(1)} + v_{2i\eta+1}^{(1)} \kappa_{2i+1}^{(1)}) \right] \\ & + \omega_{12}^2 \left[v_1^{(2)} + \frac{1}{2} \sum_{i=1}^{R} (v_{2i\eta}^{(2)} \kappa_{2i}^{(2)} + v_{2i\eta+1}^{(2)} \kappa_{2i+1}^{(2)}) \right] - f_1^{(1)}, \end{aligned} \tag{10a}$$

$$\begin{aligned} S_{2r}^{(1)} = {} & - \left(\frac{\Lambda r}{\eta}\right)^2 u_{2r}^{(1)} + 2\zeta_{11}\omega_{11} \left(\frac{\Lambda r}{\eta}\right) u_{2r+1}^{(1)} + 2\zeta_{12}\omega_{12} \left(\frac{\Lambda r}{\eta}\right) u_{2(r/n)+1}^{(2)} \\ & + \omega_{11}^2 (v_{2r}^{(1)} + v_1^{(1)} \kappa_{2r/\eta}^{(1)}) + \omega_{12}^2 (v_{2r/n}^{(2)} + v_1^{(2)} \kappa_{2r/n\eta}^{(2)}) - f_{2r/\eta}^{(1)} \\ & + \frac{\omega_{11}^2}{2} \sum_{i=1}^{R} \{\kappa_{2i}^{(1)} (v_{2(i\eta-r)}^{(1)} + v_{2(i\eta+r)}^{(1)} + v_{2(r-i\eta)}^{(1)}) \\ & + \kappa_{2i+1}^{(1)} (v_{2(i\eta-r)+1}^{(1)} + v_{2(i\eta+r)+1}^{(1)} - v_{2(r-i\eta)+1}^{(1)})\} \\ & + \frac{\omega_{12}^2}{2} \sum_{i=1}^{R} \{\kappa_{2i}^{(2)} (v_{2(i\eta-r/n)}^{(2)} + v_{2(i\eta+r/n)}^{(2)} + v_{2(r/n-i\eta)}^{(2)}) \\ & + \kappa_{2i+1}^{(2)} (v_{2(i\eta-r/n)+1}^{(2)} + v_{2(i\eta+r/n)+1}^{(2)} - v_{2(r/n-i\eta)+1}^{(2)})\}, \end{aligned} \tag{10b}$$

$$
\begin{aligned}
S_{2r+1}^{(1)} = & -\left(\frac{\Lambda r}{\eta}\right)^2 u_{2r+1}^{(1)} - 2\zeta_{11}\omega_{11}\left(\frac{\Lambda r}{\eta}\right)u_{2r}^{(1)} - 2\zeta_{12}\omega_{12}\left(\frac{\Lambda r}{\eta}\right)u_{2(r/n)}^{(2)} + \omega_{11}^2(v_1^{(1)}\kappa_{2(r/\eta)+1}^{(1)} + v_{2r+1}^{(1)}) \\
& + \omega_{12}^2(v_1^{(2)}\kappa_{2(r/n\eta)+1}^{(2)} + v_{2(r/n)+1}^{(2)}) - f_{2(r/\eta)+1}^{(1)} \\
& + \frac{\omega_{11}^2}{2}\sum_{i=1}^{R}\{\kappa_{2i}^{(1)}(-v_{2(i\eta-r)+1}^{(1)} + v_{2(i\eta+r)+1}^{(1)} + v_{2(r-i\eta)+1}^{(1)}) + \kappa_{2i+1}^{(1)}(v_{2(i\eta-r)}^{(1)} - v_{2(i\eta+r)}^{(1)} + v_{2(r-i\eta)}^{(1)})\} \\
& + \frac{\omega_{12}^2}{2}\sum_{i=1}^{R}\{\kappa_{2i}^{(2)}(-v_{2(i\eta-r/n)+1}^{(2)} + v_{2(i\eta+r/n)+1}^{(2)} + v_{2(r/n-i\eta)+1}^{(2)}) + \kappa_{2i+1}^{(2)}(v_{2(i\eta-r/n)}^{(2)} \\
& - v_{2(i\eta+r/n)}^{(2)} + v_{2(r/n-i\eta)}^{(2)})\}, \qquad (10c)
\end{aligned}
$$

$$
\begin{aligned}
S_1^{(2)} = & \omega_{21}^2\left[v_1^{(1)} + \frac{1}{2}\sum_{i=1}^{R}(v_{2(i\eta)}^{(1)}\kappa_{2i}^{(1)} + v_{2(i\eta)+1}^{(1)}\kappa_{2i+1}^{(1)})\right] \\
& + \omega_{22}^2\left[v_1^{(2)} + \frac{1}{2}\sum_{i=1}^{R}(v_{2(i\eta)}^{(2)}\kappa_{2i}^{(2)} + v_{2(i\eta)+1}^{(2)}\kappa_{2i+1}^{(2)})\right] - f_1^{(2)}, \qquad (10d)
\end{aligned}
$$

$$
\begin{aligned}
S_{2r}^{(2)} = & -\left(\frac{\Lambda r}{\eta}\right)^2 u_{2(r/n)}^{(2)} + 2\zeta_{21}\omega_{21}\left(\frac{\Lambda r}{\eta}\right)u_{2r+1}^{(1)} + 2\zeta_{22}\omega_{22}\left(\frac{\Lambda r}{\eta}\right)u_{2(r/n)+1}^{(2)} \\
& + \omega_{21}^2(v_{2r}^{(1)} + v_1^{(1)}\kappa_{2(r/\eta)}^{(1)}) + \omega_{22}^2(v_{2(r/n)}^{(2)} + v_1^{(2)}\kappa_{2(r/n\eta)}^{(2)}) - f_{2(r/\eta)}^{(2)} \\
& + \frac{\omega_{21}^2}{2}\sum_{i=1}^{R}\{\kappa_{2i}^{(1)}(v_{2(i\eta-r)}^{(1)} + v_{2(i\eta+r)}^{(1)} + v_{2(r-i\eta)}^{(1)}) + \kappa_{2i+1}^{(1)}(v_{2(i\eta-r)+1}^{(1)} \\
& + v_{2(i\eta+r)+1}^{(1)} - v_{2(r-i\eta)+1}^{(1)})\} \\
& + \frac{\omega_{22}^2}{2}\sum_{i=1}^{R}\{\kappa_{2i}^{(2)}(v_{2(i\eta-r/n)}^{(2)} + v_{2(i\eta+r/n)}^{(2)} + v_{2(r/n-i\eta)}^{(2)}) + \kappa_{2i+1}^{(2)}(v_{2(i\eta-r/n)+1}^{(2)} \\
& + v_{2(i\eta+r/n)+1}^{(2)} - v_{2(r/n-i\eta)+1}^{(2)})\}, \qquad (10e)
\end{aligned}
$$

$$
\begin{aligned}
S_{2r+1}^{(2)} = & -\left(\frac{\Lambda r}{\eta}\right)^2 u_{2(r/n)+1}^{(2)} - 2\zeta_{21}\omega_{21}\left(\frac{\Lambda r}{\eta}\right)u_{2r}^{(1)} - 2\zeta_{22}\omega_{22}\left(\frac{\Lambda r}{\eta}\right)u_{2(r/n)}^{(2)} \\
& + \omega_{21}^2(v_1^{(1)}\kappa_{2(r/\eta)+1}^{(1)} + v_{2r+1}^{(1)}) + \omega_{22}^2(v_1^{(2)}\kappa_{2(r/n\eta)+1}^{(2)} + v_{2(r/n)+1}^{(2)}) - f_{2(r/\eta)+1}^{(2)} \\
& + \frac{\omega_{21}^2}{2}\sum_{i=1}^{R}\{\kappa_{2i}^{(1)}(-v_{2(i\eta-r)+1}^{(1)} + v_{2(i\eta+r)+1}^{(1)} + v_{2(r-i\eta)+1}^{(1)}) + \kappa_{2i+1}^{(1)}(v_{2(i\eta-r)}^{(1)} - v_{2(i\eta+r)}^{(1)} + v_{2(r-i\eta)}^{(1)})\} \\
& + \frac{\omega_{22}^2}{2}\sum_{i=1}^{R}\{\kappa_{2i}^{(2)}(-v_{2(i\eta-r/n)+1}^{(2)} + v_{2(i\eta+r/n)+1}^{(2)} + v_{2(r/n-i\eta)+1}^{(2)}) \\
& + \kappa_{2i+1}^{(2)}(v_{2(i\eta-r/n)}^{(2)} - v_{2(i\eta+r/n)}^{(2)} + v_{2(r/n-i\eta)}^{(2)})\}, \qquad (10f)
\end{aligned}
$$

$$
S_{4R+3} = u_j^{(\ell)} - u^*. \qquad (10g)
$$

The last equation above ($j \in [1, 2R+1]$ and $\ell = 1$ or 2) is added in order to expedite solution through the bifurcation points. As the solution approaches (singular) bifurcation points, the control parameter can be switched from the dimensionless frequency Λ to another unknown and the other elements of the solution vector $\mathbf{u}$ and Λ can be treated as unknowns to be determined.

Table 1
Dimensional parameters of the baseline example gear pair

Parameter	Gear 1	Gear 2	Gear 3	Gear 4
Base circle radius (m)	0.10	0.05	0.10	0.05
Mass (kg)	14.81	3.7	7.4	1.85
Inertia (kg/m^2)	0.074	0.0046	0.0375	0.0023
Mean mesh stiffness (N/m)	5×10^8		2.5×10^8	
Mesh damping coefficient (Ns/m)	2721		1360	

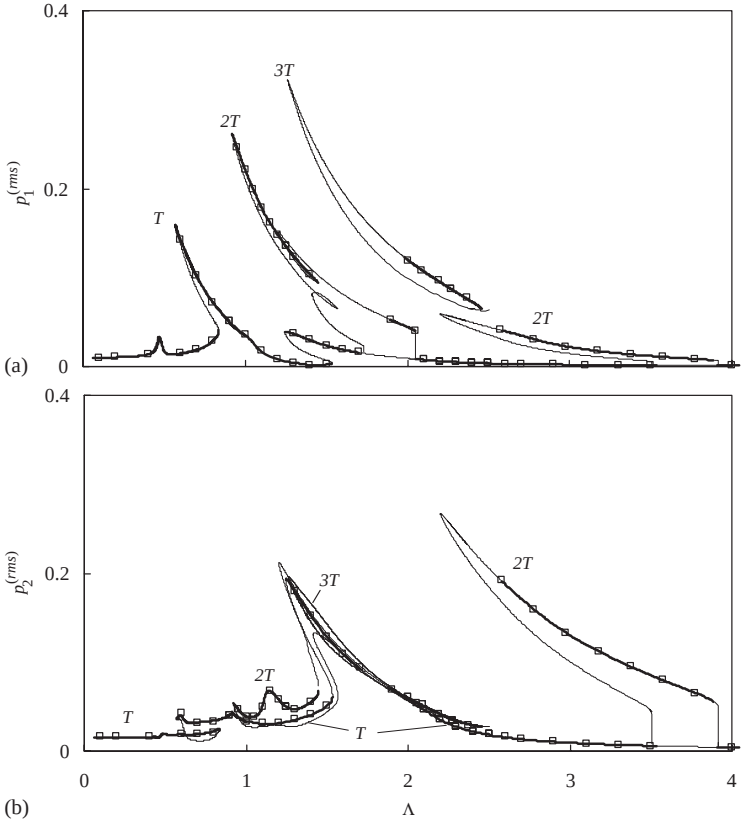

Fig. 3. Comparison of r.m.s. values of $1T$, $2T$ and $3T$ motions predicted by HBM and NI for $R = 6$, $\zeta = 0.05$, $K = 1$, $\kappa_2^{(1)} = \kappa_2^{(2)} = 0.3$, $\omega_{n2} \approx 2\omega_{n1} = 1.86$, $f_1^{(2)} = 4f_1^{(1)} = 0.185$, $b_1 = b_2 = 1$ and $b_c = 30$ μm. (—) Stable and (—) unstable HBM solutions and (□) NI solutions. (a) p_1, (b) p_2.

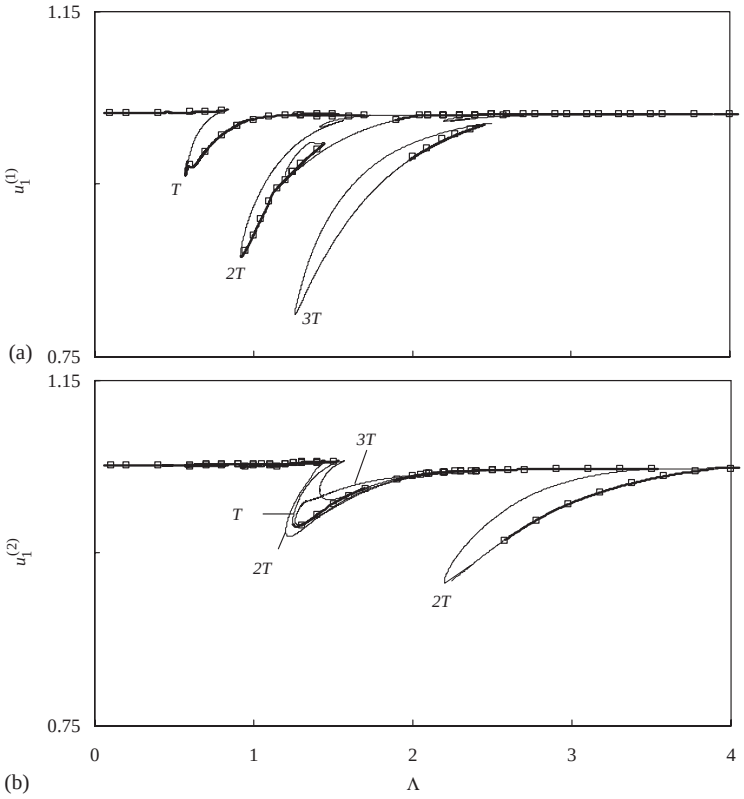

Fig. 4. Mean components of nT (a) $p_1(t)$ and (b) $p_2(t)$ motions for $R = 6$, $\zeta = 0.05$, $K = 1$, $\kappa_2^{(1)} = \kappa_2^{(2)} = 0.3$, $\omega_{n2} \approx 2\omega_{n1} = 1.86, f_1^{(2)} = 4f_1^{(1)} = 0.185$, $b_1 = b_2 = 1.0$ and $b_c = 30$ μm. (—) Stable and (—) unstable HBM solutions and (□) NI solutions.

Discrete Fourier transforms are used to represent $v_i^{(j)}$ in terms of $u_i^{(j)}$ [15,16,26]. The values of the $p_i(t)$ and $g_i(t)$ at the discrete time $t = q\rho$ (where $q \in [0, Q-1]$) are written as

$$p_{1q} = u_1^{(1)} + \sum_{r=1}^{R} \left[u_{2r}^{(1)} \cos\left(\frac{2\pi rq}{Q}\right) + u_{2r+1}^{(1)} \sin\left(\frac{2\pi rq}{Q}\right) \right], \tag{11a}$$

$$p_{2q} = u_1^{(2)} + \sum_{r=1}^{R} \left[u_{2r}^{(2)} \cos\left(\frac{2\pi rnq}{Q}\right) + u_{2r+1}^{(2)} \sin\left(\frac{2\pi rnq}{Q}\right) \right], \tag{11b}$$

and

$$g_{iq} = \begin{cases} p_{iq}(t) - b_i, & p_{iq}(t) > b_i, \\ 0, & |p_{iq}(t)| \leqslant b_i, \\ p_{iq}(t) + b_i, & p_{iq}(t) < -b_i, \end{cases} \qquad i = 1, 2, \tag{11c}$$

where $\rho = 2\pi/(Q\Lambda)$ and Q is the total number of the discrete points. Using Eqs. (11), the coefficients of $v_i^{(j)}$ can be determined by using of the inverse Fourier transforms such

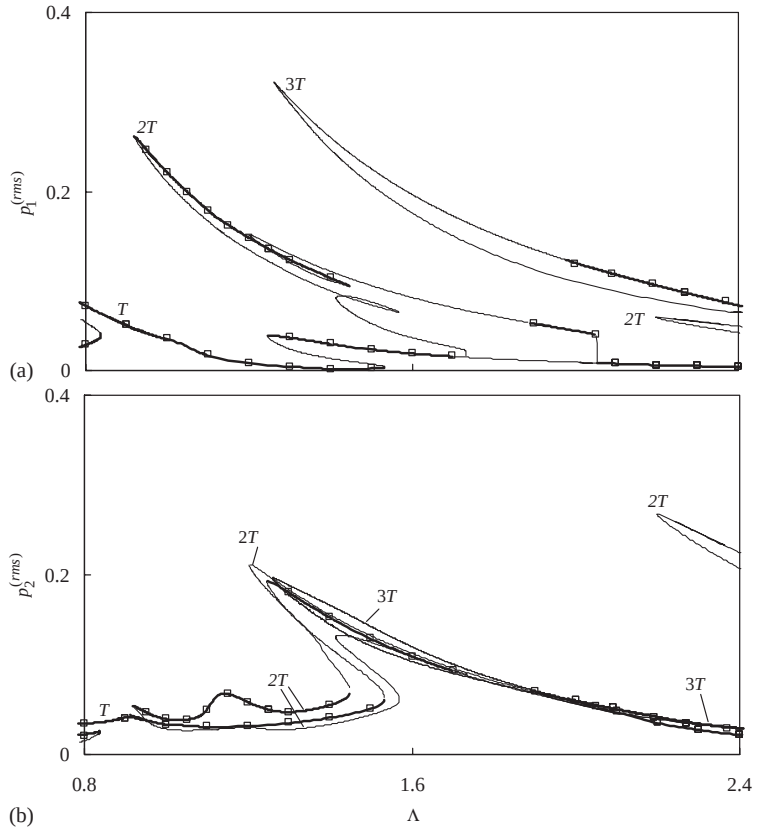

Fig. 5. An enlarged view of the r.m.s. amplitudes of nT motions shown in Fig. 3. (—) Stable and (—) unstable HBM solutions and (□) NI solutions. (a) p_1, (b) p_2.

that ($r \in [1, R]$)

$$v_1^{(1)} = \frac{1}{Q}\sum_{q=0}^{Q-1} g_{1q}, \qquad v_1^{(2)} = \frac{1}{Q}\sum_{q=0}^{Q-1} g_{2q}, \tag{12a, b}$$

$$v_{2r}^{(1)} = \frac{2}{Q}\sum_{q=0}^{Q-1} g_{1q}\cos\left(\frac{2\pi rq}{Q}\right), \qquad v_{2r}^{(2)} = \frac{2}{Q}\sum_{q=0}^{Q-1} g_{2q}\cos\left(\frac{2\pi rnq}{Q}\right), \tag{12c, d}$$

$$v_{2r+1}^{(1)} = \frac{2}{Q}\sum_{q=0}^{Q-1} g_{1q}\sin\left(\frac{2\pi rq}{Q}\right), \qquad v_{2r+1}^{(2)} = \frac{2}{Q}\sum_{q=0}^{Q-1} g_{2q}\sin\left(\frac{2\pi rnq}{Q}\right). \tag{12e, f}$$

Above values of $v_i^{(j)}$ are substituted into Eq. (10) to obtain $(4R + 3)$ non-linear algebraic equations that can be solved for $\mathbf{U}$ using the Newton–Raphson method according to

$$\mathbf{U}^{(m)} = \mathbf{U}^{(m-1)} - (\mathbf{J}^{-1})^{(m-1)}\mathbf{S}^{(m-1)}. \tag{13}$$

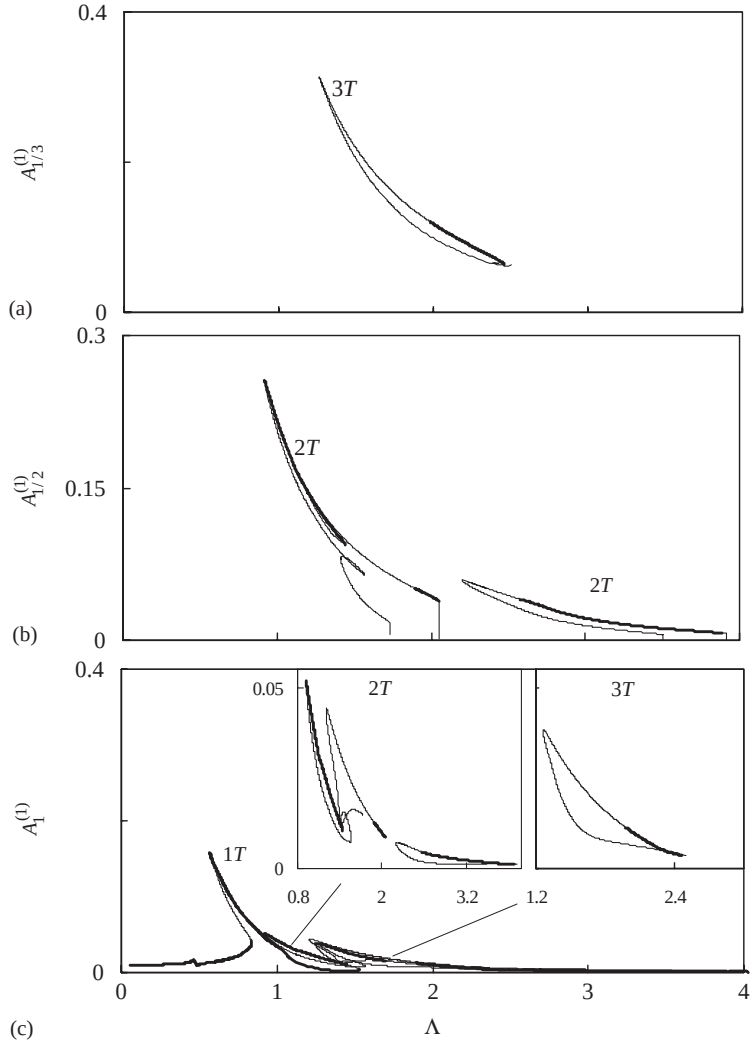

Fig. 6. Harmonic amplitudes (a) $A^{(1)}_{1/3}$, (b) $A^{(1)}_{1/2}$ and (c) $A^{(1)}_1$ corresponding to Fig. 3(a). (—) Stable and (—) unstable HBM solutions.

Here, superscript m is an index for iterations and $\mathbf{J}^{-1}$ is the inverse of the Jacobian matrix of the vector $\mathbf{S}$ estimated at the previous iteration values. Starting with an initial guess $\mathbf{U}^{(0)}$ and a control parameter set to u^* (say Λ), the iteration of Eq. (13) is repeated until the steady state solution $\mathbf{U}^{(m)}$ converges within a certain predefined error limit. The control parameter is set to the next value of interest by increasing or decreasing u^* until a bifurcation point impedes continuation. Then, another unknown is adapted as the new control parameter. The individual elements of $\mathbf{J}$ in Eq. (13) are given in Appendix A. Finally, the Floquet theory is used to determine is the stability of the HBM solutions [26].

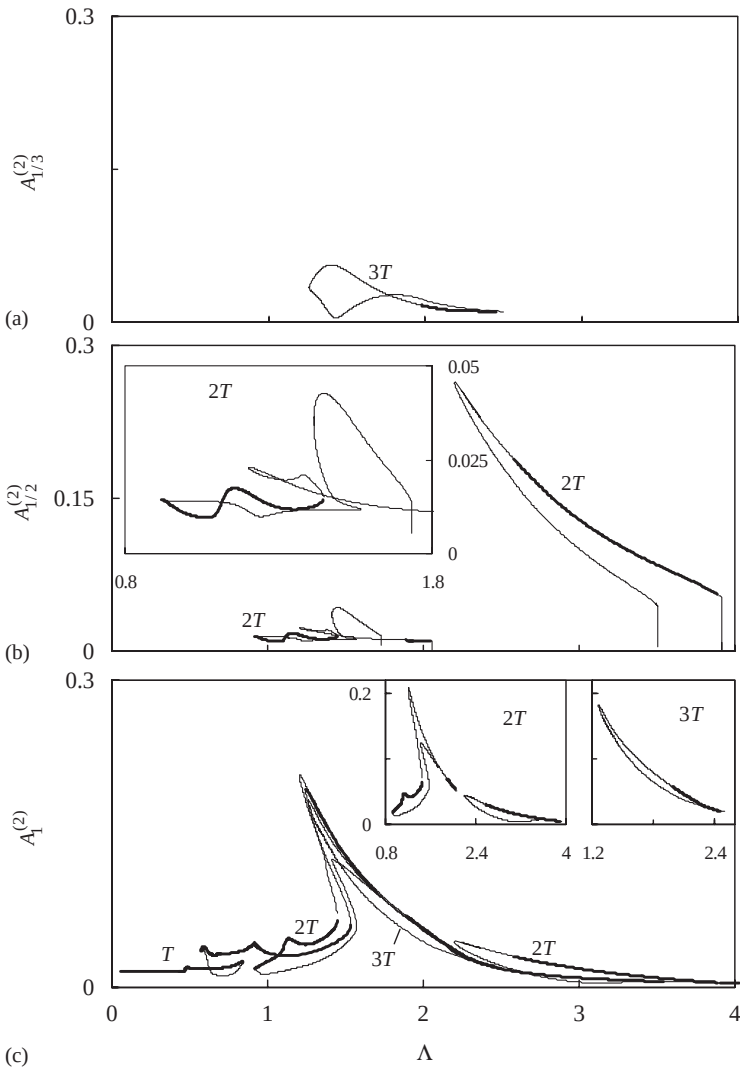

Fig. 7. Harmonic amplitudes (a) $A^{(2)}_{1/3}$, (b) $A^{(2)}_{1/2}$ and (c) $A^{(2)}_{1}$ corresponding to Fig. 3(b). (—) Stable and (—) unstable HBM solutions.

4. Results and discussion

A HBM solution similar to the one proposed above was used successfully to predict $1T$ motions of the same gear train [26]. In that study, $1T$ solutions were shown to become unstable near regions of parametric resonances. NI method was used in these regions to show that these regions are indeed dictated by stable sub-harmonic motions. These nT motions will be predicted analytically in this study for the same gear train example of Ref. [26]. The parameters of the example system are listed in Table 1. The dimensionless system parameters are calculated by using these dimensional parameters and the relationships given in Section 2.

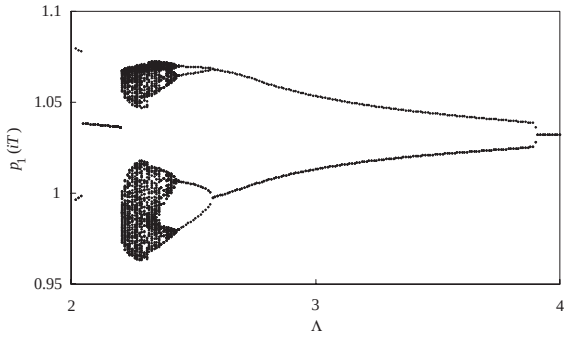

Fig. 8. Bifurcation diagram of stable nT and chaotic motions of Fig. 3(a) within $\Lambda \in [2.0, 4.0]$.

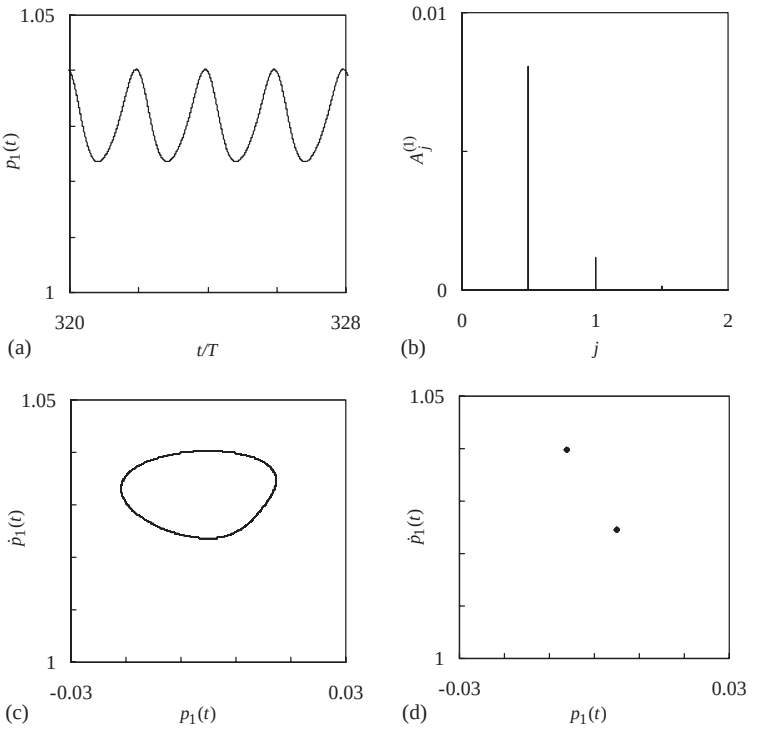

Fig. 9. $2T$ motion of Fig. 3(a) at $\Lambda = 3.8$; (a) $p_1(t)$ versus time, (b) the FFT spectrum, (c) the phase plane plot and (d) the Poincaré map.

A large number of parameters define the system dynamically. In order to limit the parameter set, only the fundamental harmonics of the mesh stiffness functions $\kappa_1(t)$ and $\kappa_2(t)$ are considered here by setting $K = 1$ in Eq. (6) so that the mesh stiffness functions are harmonic. Similarly, constant external forces were considered to account for the mean force transmitted, while torque pulsations and kinematic gear transmission errors are not included in this parametric study ($\bar{T}_1(\bar{t})$

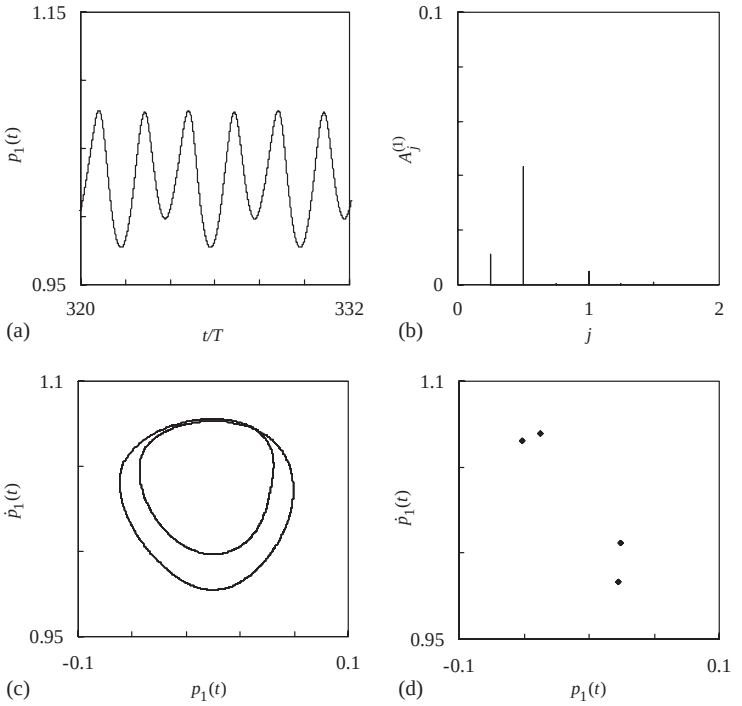

Fig. 10. $4T$ motion at $\Lambda = 2.475$ of Fig. 3(a); (a) $p_1(t)$ versus time, (b) the FFT spectrum, (c) the phase plane plot and (d) the Poincaré map.

and $\bar{T}_4(\bar{t})$ are constants and $e_1(\bar{t}) = e_2(\bar{t}) = 0$) resulting in constant $f_1(t)$ and $f_2(t)$ in Eqs. (5c,d). Further, gears 2 and 3 have the same number of teeth, $n = Z_2/Z_3 = 1$.

4.1. Comparison to NI results

Fig. 3 compares a set of nT sub-harmonic motions obtained by HBM to those obtained by direct NI. These solutions were obtained by assuming a six-term steady state solution, $R = 6$ in Eq. (7), and letting $\eta \leqslant 3$. A damping ratio value of $\zeta = 0.05$ is considered where $\zeta = c_1/2\sqrt{k_{1m}m_{12}} = c_2/2\sqrt{k_{2m}m_{34}}$, $m_{ij} = I_iI_j/(r_i^2I_j + r_j^2I_i)$. Harmonic gear mesh stiffness amplitudes of $\kappa_2^{(1)} = \kappa_2^{(2)} = 0.3$ correspond to a theoretical involute contact ratio value of 1.7 [26]. In addition, $f_1^{(2)} = 4f_1^{(1)} = 0.184$ corresponds to an input torque value of $T_1 = 100$ Nm. A characteristic length of $b_c = 30$ μm is considered with $b_1 = b_2 = 1$. The value of the characteristic frequency is set to $\omega_c = \bar{\omega}_{11} = 9874$ rad/s. As in Ref. [26], the undamped natural frequencies of the system defined in Table 1 are $\omega_{n1} = 0.96$ and $\omega_{n2} = 1.86$. The root-mean-square (r.m.s.) values $p_1(t)$ and $p_2(t)$ are defined as

$$p_j^{(\mathrm{r.m.s.})} = \left\{ \sum_{r=1}^{R} [A_{r/\eta}^{(j)}]^2 \right\}^{1/2}, \tag{14a}$$

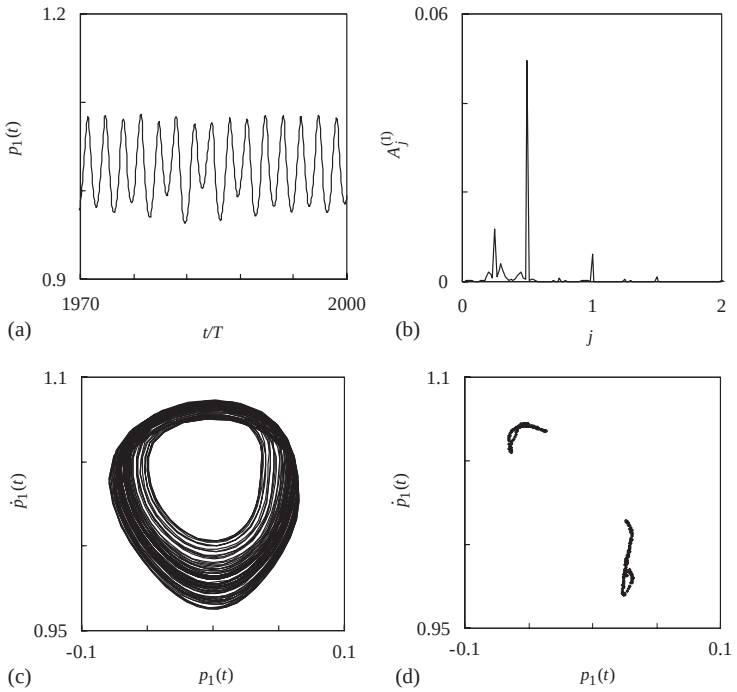

Fig. 11. Chaotic motion at $\Lambda = 2.35$ of Fig. 3(a); (a) $p_1(t)$ versus time, (b) the FFT spectrum, (c) the phase plane plot and (d) the Poincaré map.

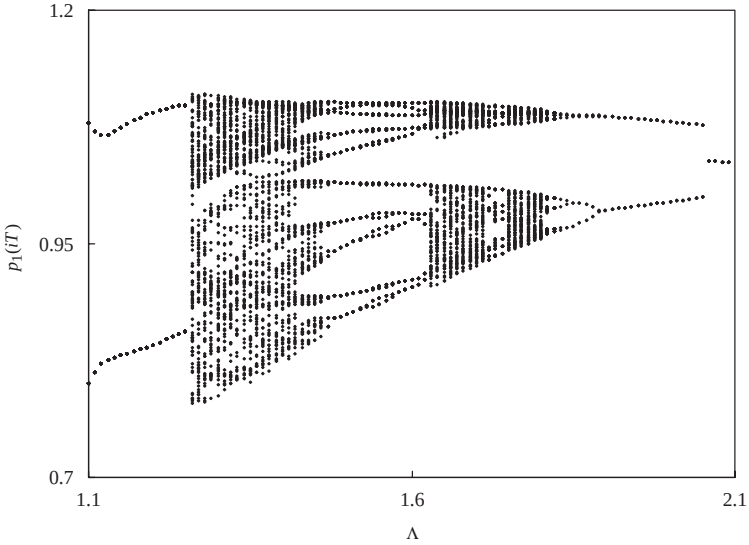

Fig. 12. Bifurcation diagram of stable nT motions of Fig. 3(a) within $\Lambda \in [1.1, 2.1]$.

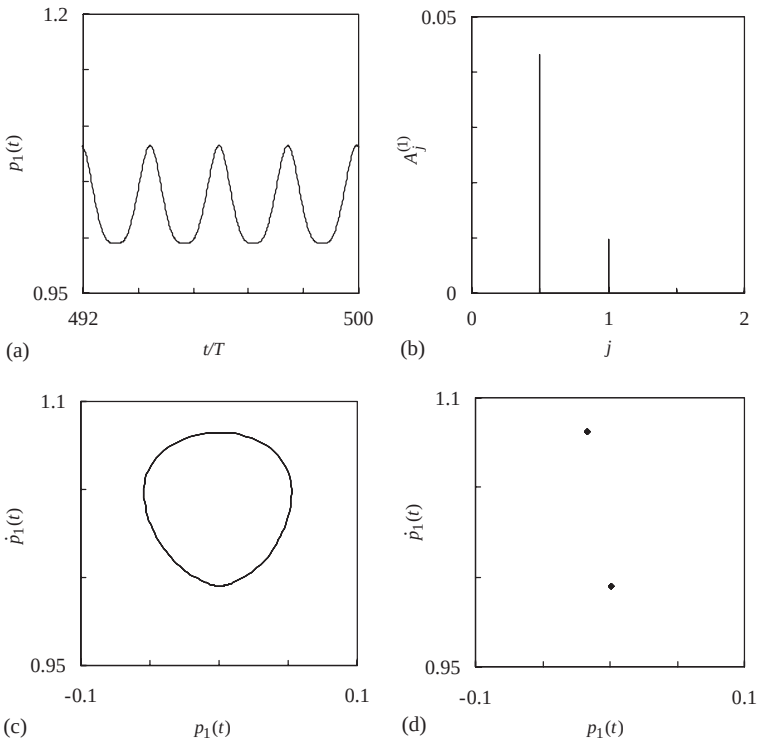

Fig. 13. $2T$ motion of Fig. 3(a) at $\Lambda = 2$; (a) $p_1(t)$ versus time, (b) the FFT spectrum, (c) the phase plane plot and (d) the Poincaré map.

where $A_{r/\eta}^{(j)}$ is the amplitude of the r/ηth component of $p_j(t)$ that is defined as

$$A_{r/\eta}^{(j)} = \{[u_{2r}^{(j)}]^2 + [u_{2r+1}^{(j)}]^2\}^{1/2}. \tag{14b}$$

In Fig. 3(a), $p_1^{(\text{r.m.s.})}$ is plotted as a function of Λ including (stable and unstable) $1T$, $2T$ and $3T$ motions. Stable and unstable HBM solutions are shown by thick and thin lines, respectively. In addition, square symbols represent the NI solutions obtained by varying the initial conditions to converge to the desired solutions in the multi-valued stable solution regions. The HBM and NI solutions agree well, indicating that the HBM is accurate in predicting both $1T$ and nT motions. Such an agreement is evident in Figs. 3(b) and 4 for $p_2^{(\text{r.m.s.})}$ and mean components of $p_1(t)$ and $p_2(t)$ as well.

In Fig. 3, the $1T$ motions within the frequency ranges $\Lambda \in (1.76, 2.05)$ and $\Lambda \in (3.5, 3.92)$ are unstable. These ranges correspond to fundamental parametric instabilities of $\Lambda \approx 2\omega_{n1}$ and $\Lambda \approx 2\omega_{n2}$, respectively. In these regions, stable sub-harmonic motions take over, preventing any very large amplitude vibrations. For instance, as Λ is reduced from 4.0, the $1T$ motion loses its stability and a jump-up to a stable $2T$ motion takes place at $\Lambda = 3.92$. The forced response curve of this $2T$ sub-harmonic resonance follows a softening type bend to the left, primarily due to the tooth separations. Within $\Lambda \in (3.5, 3.92)$, $2T$ motions are the only stable solutions exhibiting tooth

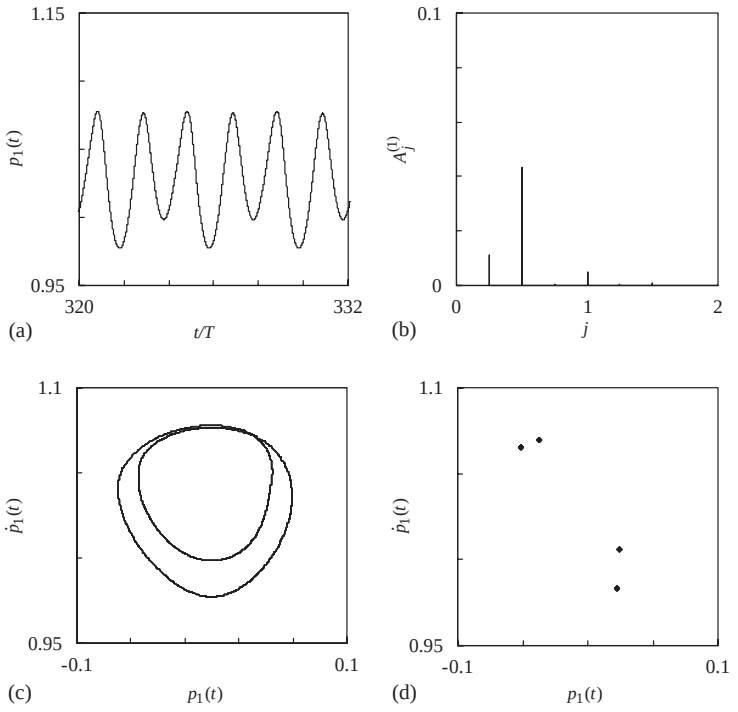

Fig. 14. $4T$ motion of Fig. 3(a) at $\Lambda = 1.85$; (a) $p_1(t)$ versus time, (b) the FFT spectrum, (c) the phase plane plot and (d) the Poincaré map.

separations (single-sided impacts) while linear $1T$ (no impact) and $2T$ motions coexist within $\Lambda \in (3.5, 2.57)$. Similarly, by reducing Λ beyond 2.05 near $\Lambda \approx 2\omega_{n1}$ causes similar bifurcations that results in a jump-up from a stable $1T$ to a stable $2T$ motion or a $3T$ motion. The curves representing the $2T$ sub-harmonic resonance also exhibit a softening type non-linear behavior. However, the shape of this curve is rather complicated since the primary resonance frequency $\Lambda \approx \omega_{n2}$ coincides with the fundamental parametric resonance frequency $\Lambda \approx 2\omega_{n1}$. A zoomed view of the same $2T$ motions within $\Lambda \in (0.8, 2.4)$ shown in Fig. 5 reveal that several bifurcations take place on this $2T$ branch.

A $3T$ sub-harmonic resonance curve, also of softening type as shown in Fig. 3, is located on top of the $2T$ curve. This is the sub-harmonic resonance corresponding to $\Lambda \approx 3\omega_{n1}$. While $1T$ motions lose their stability near $\Lambda \approx 2\omega_{n1}$ making the $2T$ motions unavoidable, this is not the case for the $3T$ resonance. Here, the $1T$ motions remain stable near $\Lambda \approx 3\omega_{n1}$, and hence $3T$ motions form an island and are not connected to the $1T$ motions. Therefore, these $3T$ motions should not be easily observed in real life as changing Λ is not sufficient to obtain them.

The forced response curves of $A_{1/3}^{(j)}$, $A_{1/2}^{(j)}$ and $A_1^{(j)}$ are shown in Fig. 6 and 7 ($j = 1, 2$) for the same system as Fig. 3. These figures demonstrate further that the solutions marked as $2T$ and $3T$ motions are dominated by $A_{1/2}^{(j)}$ and $A_{1/3}^{(j)}$ components of the frequency spectrum, respectively, while the primary resonances of $1T$ motions are mostly defined by $A_1^{(j)}$.

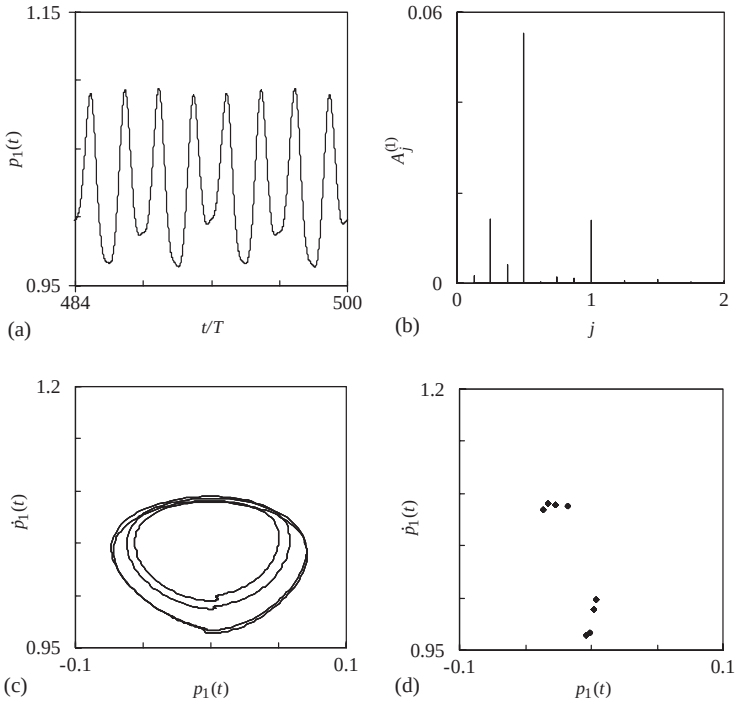

Fig. 15. $8T$ motion of Fig. 3(a) at $\Lambda = 1.825$; (a) $p_1(t)$ versus time, (b) the FFT spectrum, (c) the phase plane plot and (d) the Poincaré map.

4.2. *Long-period sub-harmonic and chaotic motions*

One other observation from Fig. 3 is that the stable $2T$ motions become unstable at $\Lambda = 2.57$ and 1.89 as Λ is reduced on the upper $2T$ branches. At $\Lambda = 2.57$, a jump-down to the stable $1T$ motion does not take place when the $2T$ solution becomes unstable. Instead, a set of bifurcations occurs to form other long-period nT motions at amplitudes comparable to the unstable $2T$ motion. The bifurcation diagram presented in Fig. 8 is obtained by reducing Λ incrementally from $\Lambda = 4$ to 2 and taking the steady state solution from the previous frequency increment as the initial guess in Eq. (13). Here, the $2T$ motion bifurcates to $4T$ motions at $\Lambda = 2.57$ through a typical period-doubling bifurcation. Further reducing the frequency, a chaotic motion is obtained at $\Lambda = 2.4$. Figs. 9–11 show $2T$, $4T$ and chaotic motions at $\Lambda = 3.8$, 2.475 and 2.35, respectively. In Fig. 9(a) and 10(a), the time histories (normalized by the mesh period $T = 1/\Lambda$) illustrate that the motions repeat themselves at every two and four mesh periods, respectively. The $2T$ motions have a large $\frac{1}{2}$ order in FFT spectrum of Fig. 9(b) while a tangible $\frac{1}{4}$ order is also evident in Fig. 10(b) for the $4T$ motion. The Poincare maps of Figs. 9(d) and 10(d) contain two and four discrete points, respectively, further demonstrating that these are indeed $2T$ and $4T$ motions. Meanwhile, in Fig. 11, the time history is not periodic, the FFT spectrum has a broadband content, and the phase plane and Poincare maps point to an apparent strange attractor indicating

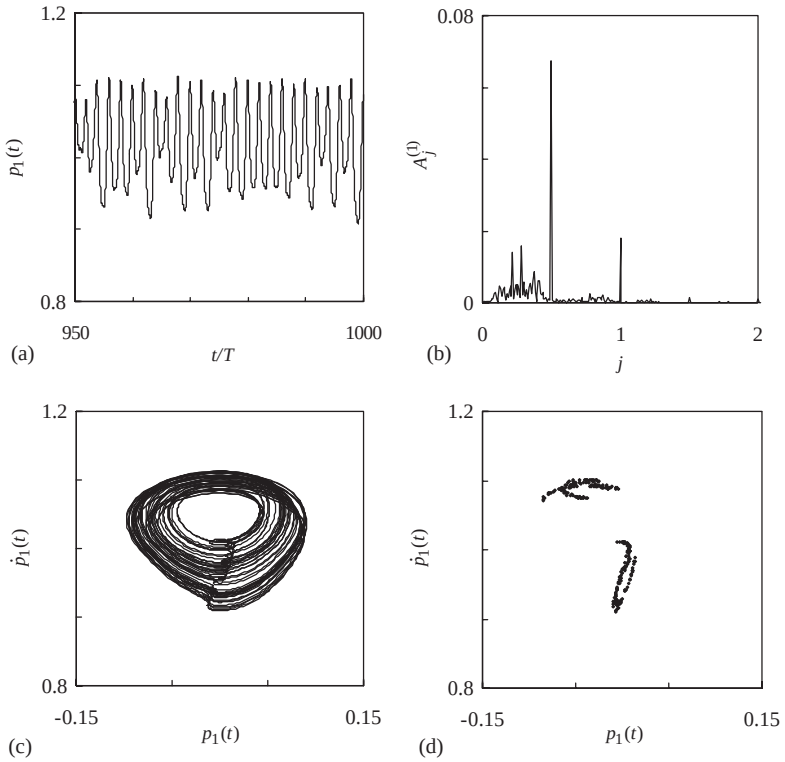

Fig. 16. Chaotic motion of Fig. 3(a) at $\Lambda = 1.65$; (a) $p_1(t)$ versus time, (b) the FFT spectrum, (c) the phase plane plot and (d) the Poincaré map.

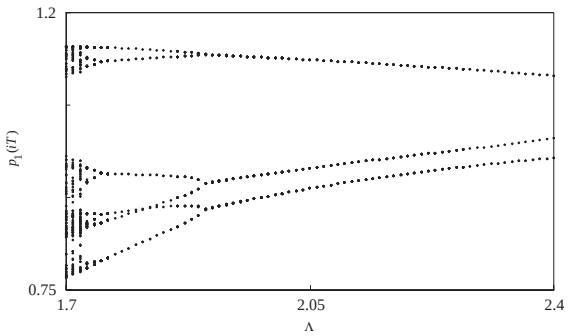

Fig. 17. Bifurcation diagram of stable nT motions of Fig. 3(a) within $\Lambda \in [1.1, 2.1]$.

that the motion is chaotic. Similarly, Fig. 13 shows a bifurcation diagram obtained on the upper branch $2T$ curve of Fig. 3 by reducing Λ from 2.1 to 1.1 gradually. A number of period-doubling bifurcations take place to form a well-defined $2^m T$ route to chaos ($2 \rightarrow 4 \rightarrow 8 \rightarrow \cdots \rightarrow chaos$) within $\Lambda \in (1.625, 2.05)$. Figs. 13–16 illustrate examples of $2T$, $4T$, $8T$ and chaotic motions within this

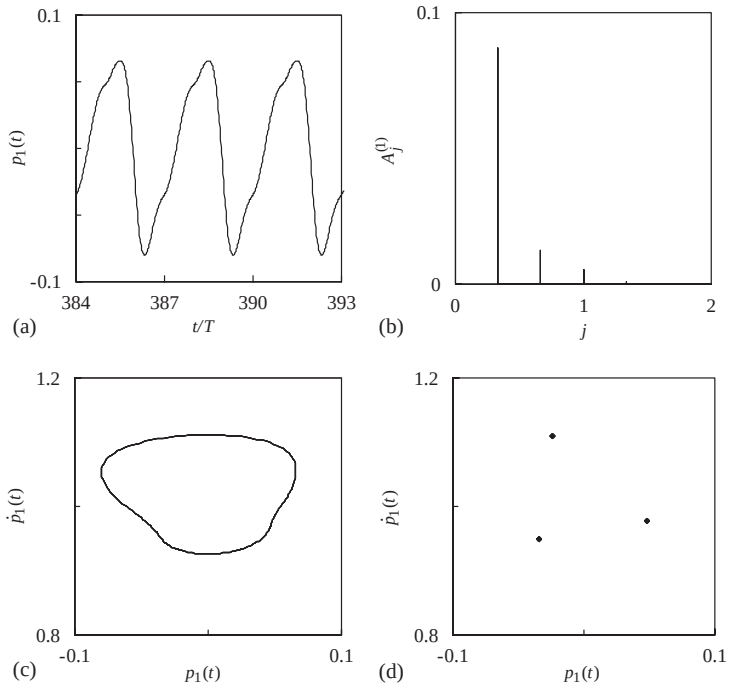

Fig. 18. $3T$ motion of Fig. 3(a) at $\Lambda = 2.2605$; (a) $p_1(t)$ versus time, (b) the FFT spectrum, (c) the phase plane plot and (d) the Poincaré map.

frequency range. In Fig. 12, other long-period sub-harmonic motions such as $5(2^m)T$ motions also exist between the frequency bands of chaotic motion.

In the same fashion, $3T$ motions lose their stability at $\Lambda = 1.96$ as Λ is reduced. A bifurcation diagram of this branch of $3T$ motions shown in Fig. 17 indicates that, at $\Lambda = 1.96$, the $3T$ motions bifurcate to $6T$ motions. What follows is a $3(2^m)T$ period-doubling cascade leading to chaotic behavior. Figs. 18–21 illustrate $3T$, $6T$, $12T$ and chaotic motions at $\Lambda = 2.26$, 1.87, 1.74 and 1.72, respectively.

It is also worthwhile to point out in Fig. 3 that more than one stable nT motions coexist at certain Λ values. For instance, at $\Lambda = 1.35$, there are three such motions, namely two stable $1T$ motions (one linear and one single-sided impact) and one stable $2T$ motion. As Λ is increased to 1.5, a jump-up takes place, while the resultant stable motion will be either the other upper branch $1T$ motion or a sub-harmonic motion. In this case, the initial conditions at the point of jump-up should determine the type of the resultant motion.

4.3. *Influence of system parameters*

Influence of the mean force transmitted by the gear train on the steady state $2T$ response is shown in Fig. 22. Here, the same system as Fig. 3 considered under torque values of $T = 50$, 100 and 150 Nm. As reported earlier for $1T$ motions [26], increasing the mean force fails to prevent tooth separations from occurring. The qualitative shape of the $p_1^{(\text{r.m.s.})}$ and $p_2^{(\text{r.m.s.})}$ curves remain

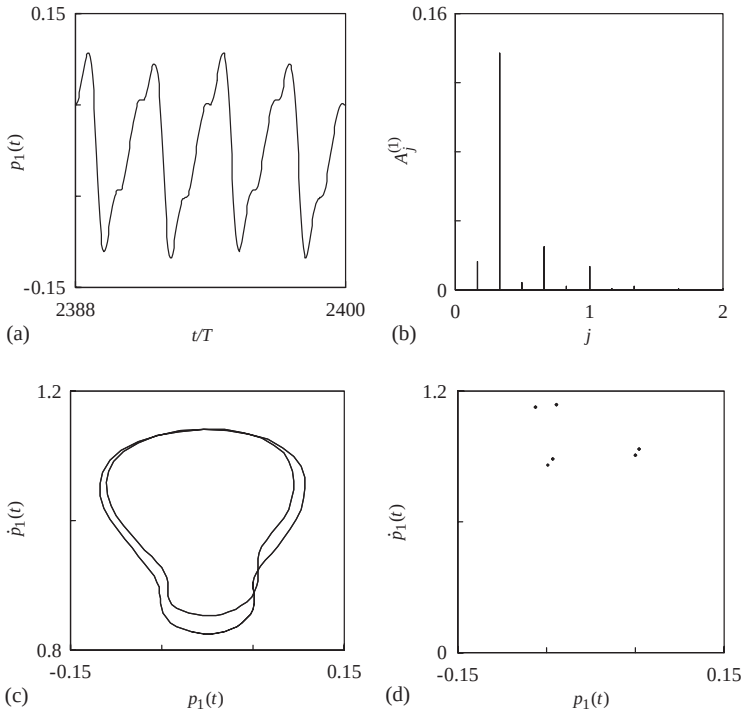

Fig. 19. $6T$ motion of Fig. 3(a) at $\Lambda = 1.870$; (a) $p_1(t)$ versus time, (b) the FFT spectrum, (c) the phase plane plot and (d) the Poincaré map.

the same while the overall amplitudes are elevated with increasing mean force values $f_1^{(1)}$ and $f_1^{(2)}$. It is also noted that the frequencies ranges in which the $2T$ motions become unstable are not influenced by the $f_1^{(1)}$ and $f_1^{(2)}$.

The influence of the damping ratio on the $p_1^{(\text{r.m.s.})}$ and $p_2^{(\text{r.m.s.})}$ response curves of $2T$ and $3T$ motions near one of the fundamental parametric resonances within $\Lambda \in [1.5, 6]$ is shown in Fig. 23. Here, the backlash values are reduced to $b_1 = b_2 = \frac{1}{3}$ in order to demonstrate double-sided impact motions characterized by tooth separations followed by back collisions. Double-sided impact motions were shown to exist for this system for $1T$ motions only when the system is lightly damped [26]. The $2T$ response curves corresponding to three levels of damping $\zeta = 0.075,\ 0.05$ and 0.02 demonstrate the influence of the damping values on the sub-harmonic response is very significant. While the damping value does not influence the amplitude of $2T$ single-sided impact motions at any given Λ, it affects the extent of these motions. For instance, when $\zeta = 0.075$, $2T$ motions range between $\Lambda = 3.0$ and 3.72, almost all of which are stable. This range is extended to $\Lambda \in (2.2, 3.92)$ for $\zeta = 0.05$. In both cases, the $2T$ motion maintains its stability until it reaches to its maximum point. When the damping ratio is lower, $\zeta = 0.02$, the vibration amplitudes become large enough for gears 1 and 4 to move across the entire backlash zone relative to their mating gears on the middle shaft to initiate back contact. This causes a hardening-type response curve bent to the right that starts the end of the lower $2T$ branch at $\Lambda \approx 1.79$. Lower branch $2T$ motions become unstable at $\Lambda \approx 2.75$, bifurcating to long-period nT motions as in Figs. 8, 12 and 17.

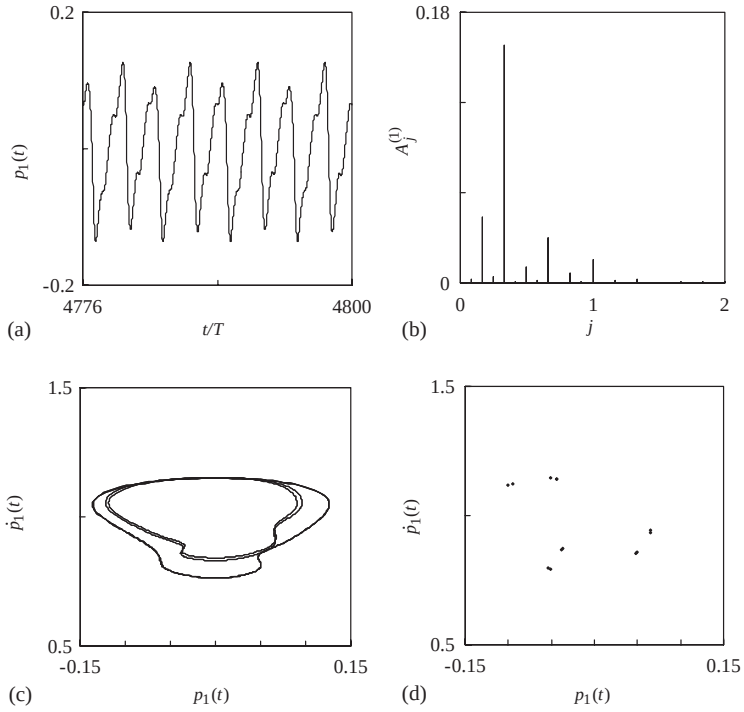

Fig. 20. $12T$ motion of Fig. 3(a) at $\Lambda = 1.740$; (a) $p_1(t)$ versus time, (b) the FFT spectrum, (c) the phase plane plot and (d) the Poincaré map.

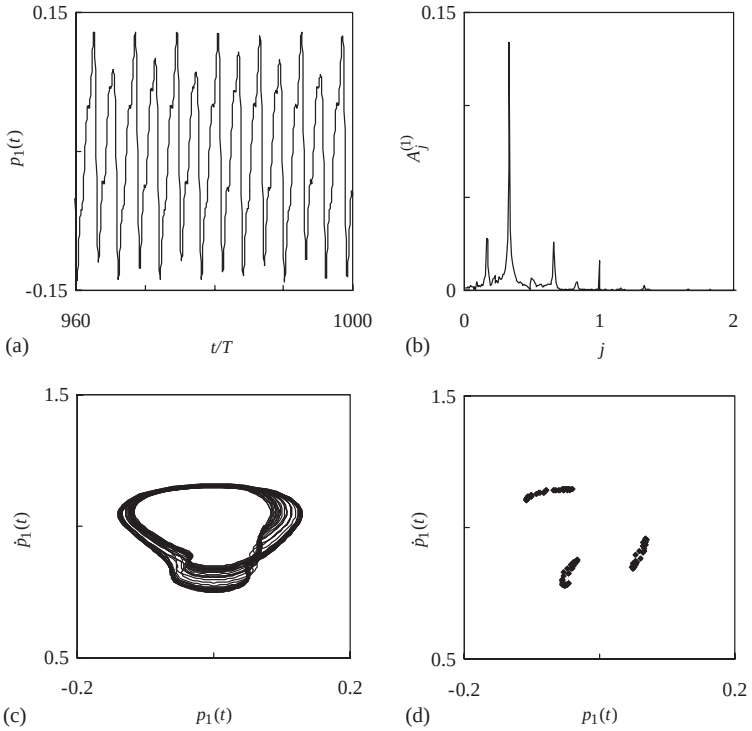

Fig. 21. Chaotic motion of Fig. 3(a) at $\Lambda = 1.720$; (a) $p_1(t)$ versus time, (b) the FFT spectrum, (c) the phase plane plot and (d) the Poincaré map.

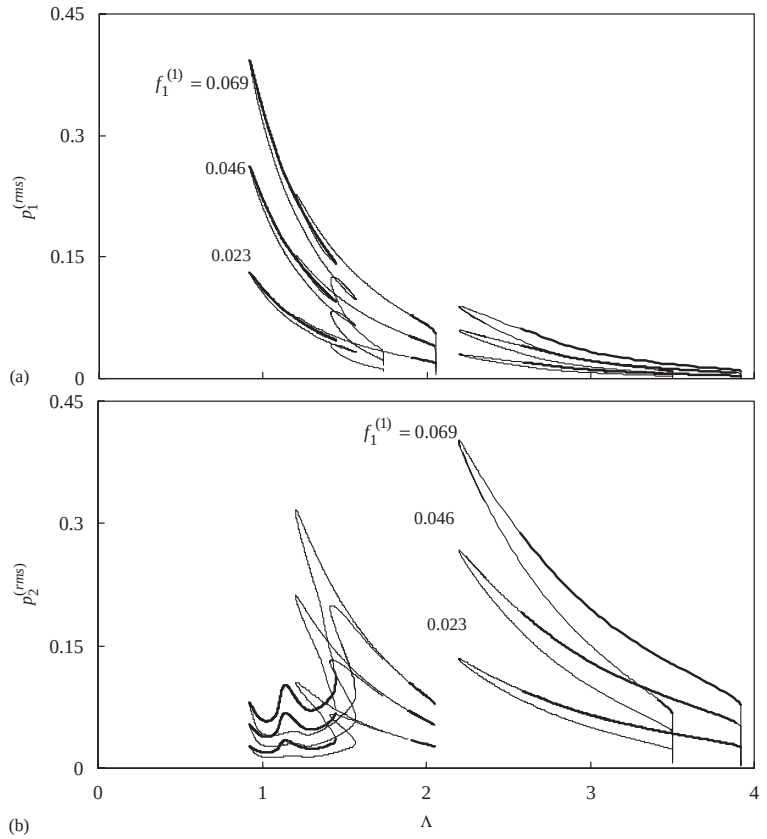

Fig. 22. $2T$ motions at different $f_1^{(2)} = 4f_1^{(1)}$ values for $R = 6$, $\zeta = 0.05$, $K = 1$, $\kappa_2^{(1)} = \kappa_2^{(2)} = 0.3$, $\omega_{n2} \approx 2\omega_{n1} = 1.86$, $b_1 = b_2 = 1$ and $b_c = 30$ μm. (—) Stable and (—) unstable HBM solutions. (a) p_1, (b) p_2.

Similarly, a boomerang-shaped island of $3T$ motions are shown at two damping values of $\zeta = 0.02$ and 0.03 exhibiting stable single-sided and unstable double-sided impact motions. When the damping ratios are increased beyond the values used in Fig. 23, say $\zeta \geqslant 0.1$, the sub-harmonic motions become more limited in both range and amplitude as the system tends to behave in a linear fashion in most of the Λ ranges. This is consistent with the findings of earlier studies using non-linear time-varying single pair models [16] and linear time-varying multi-mesh models [22].

The influence of the amplitude of harmonic mesh stiffness excitations on $2T$ sub-harmonic resonances is illustrated in Fig. 24. Here, a damping value of $\zeta = 0.05$ is used as in Fig. 3. Three different values of harmonic stiffness amplitudes are considered, $\kappa_2^{(1)} = \kappa_2^{(2)} = 0.42$, 0.3 and 0.2. These values represent the fundamental harmonic amplitudes of the mesh stiffness function for gear pairs having an involute contact ratio of 1.5, 1.7 and 1.8, respectively. Both $p_1^{(\text{r.m.s.})}$ and $p_2^{(\text{r.m.s.})}$ amplitudes of $2T$ motions decrease significantly when $\kappa_2^{(1)} = \kappa_2^{(2)}$ values are decreased. For $\kappa_2^{(1)} = \kappa_2^{(2)} = 0.42$, the response amplitudes are somewhat larger at a given Λ. However, $2T$ motions bifurcate to other nT motions at lower frequencies. For instance, $p_2^{(\text{r.m.s.})}$ values of the stable motion reach only amplitude of 0.17 before it bifurcates to a $4T$ motion. For lower stiffness

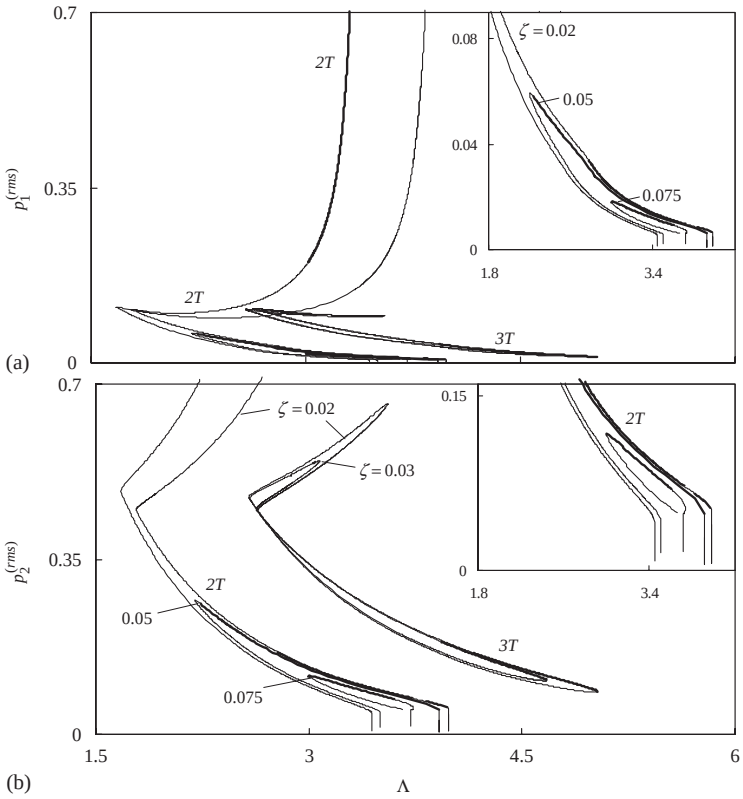

Fig. 23. $2T$ and $3T$ motions at various ζ values within $1.5 < \Lambda < 4$ for $R = 6$, $K = 1$, $\kappa_2^{(1)} = \kappa_2^{(2)} = 0.3$, $\omega_{n2} \approx 2\omega_{n1} = 1.86$, $f_1^{(2)} = 4f_1^{(1)}$, $b_1 = b_2 = \frac{1}{3}$ and $b_c = 30$ μm. (—) Stable and (—) unstable HBM solutions. (a) p_1, (b) p_2.

values, say $\kappa_2^{(1)} = \kappa_2^{(2)} = 0.3$, the response amplitudes are smaller and the frequency range of the stable $2T$ motions get slightly larger. The entire frequency range (stable and unstable) of solutions shrinks, and stable and unstable curves come closer. Further decreasing the value of the mesh stiffness amplitude to $\kappa_2^{(1)} = \kappa_2^{(2)} = 0.2$, the solution curve near $\Lambda \approx 2\omega_{n2}$ forms a closed loop. It is no longer linked lower branch $1T$ motions that are not shown in Fig. 24. As the $3T$ motions in Fig. 3, the only way to reach these $2T$ motions is some sort of a disturbance on the system beyond changing the value of Λ.

5. Conclusion

In this study, a non-linear time-varying dynamic model was employed to investigate sub-harmonic and chaotic motions exhibited by a typical multi-mesh gear train. A lumped-parameter torsional dynamic model of a system formed by three rigid shafts connected each other by two spur gear meshes was proposed. The dynamic model includes the gear backlash clearances, the parametric gear mesh stiffness fluctuations and periodic external excitations. Steady state

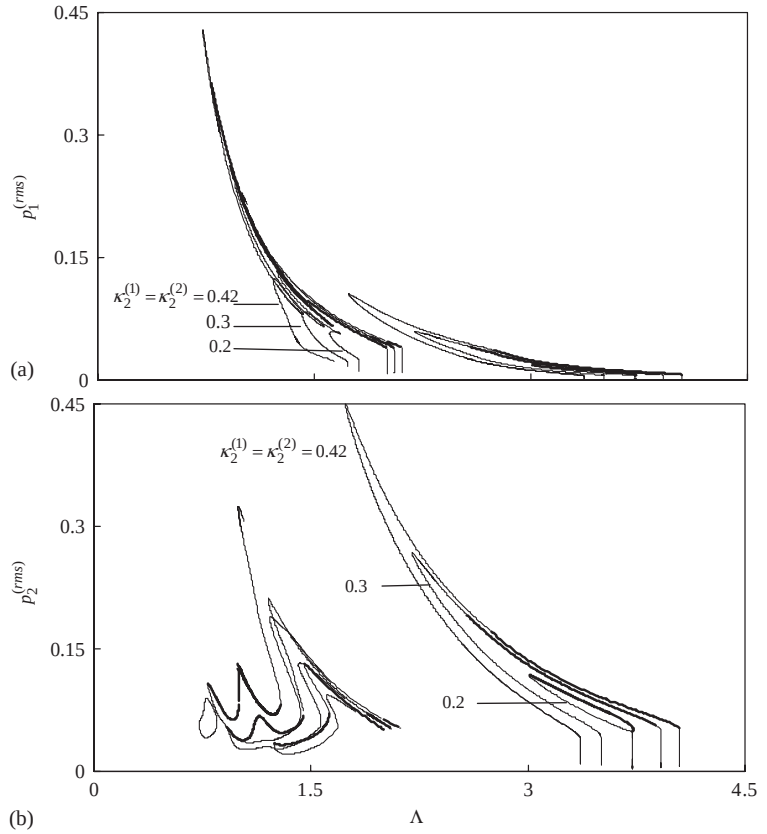

Fig. 24. $2T$ motions at various $\kappa_2^{(1)} = \kappa_2^{(2)}$ values for $R = 6$, $K = 1$, $\zeta = 0.05$, $\omega_{n2} \approx 2\omega_{n1} = 1.86$, $f_1^{(2)} = 4f_1^{(1)} = 0.185$, $b_1 = b_2 = 1$ and $b_c = 30$ μm. (—) Stable and (—) unstable HBM solutions. (a) p_1, (b) p_2.

sub-harmonic motions of the same system were studied analytically by using a multi-term HBM in conjunction with discrete Fourier transforms. The HBM predictions were shown to be in excellent agreement with direct NI results. Both $2T$ and $3T$ sub-harmonic resonances were predicted analytically and the impact of key system parameters on these resonances was quantified. These parameters included alternating mesh stiffness amplitudes, gear mesh damping and static torque transmitted. It was shown clearly that stable sub-harmonic motions, highlighting major shortcoming of earlier linear time-varying models, dictate the frequency ranges in which the period-one motions are unstable due to parametric excitations. Other non-linear phenomena including long-period sub-harmonic motions and several period doubling routes to chaos were also shown to exist quite commonly.

Acknowledgements

The authors thank Hashemite University, Jordan and the University of Toledo for supporting the first author during this study.

Appendix A. Elements of the Jacobian matrix

The individual elements of the Jacobian matrix, $\partial S_i^{(\ell)}/\partial u_j^{(\ell)}$ and $\partial S_{4R+3}/\partial \Lambda$ where $\Lambda = u_{4R+3}$, $i \in [1, R]$, $j \in [1, 2R+1]$ and $\ell = 1, 2$ are given as

$$\frac{\partial S_1^{(1)}}{\partial u_j^{(\ell)}} = \omega_{11}^2 \left[\frac{\partial v_1^{(1)}}{\partial u_j^{(\ell)}} + \frac{1}{2} \sum_{i=1}^{R} \left(\kappa_{2i}^{(1)} \frac{\partial v_{2i\eta}^{(1)}}{\partial u_j^{(\ell)}} + \kappa_{2i+1}^{(1)} \frac{\partial v_{2i\eta+1}^{(1)}}{\partial u_j^{(\ell)}} \right) \right] + \omega_{12}^2 \left[\frac{\partial v_1^{(2)}}{\partial u_j^{(\ell)}} + \frac{1}{2} \sum_{i=1}^{R} \left(\kappa_{2i}^{(2)} \frac{\partial v_{2i\eta}^{(2)}}{\partial u_j^{(\ell)}} + \kappa_{2i+1}^{(2)} \frac{\partial v_{2i\eta+1}^{(2)}}{\partial u_j^{(\ell)}} \right) \right], \tag{A.1}$$

$$\frac{\partial S_1^{(1)}}{\partial \Lambda} = \omega_{11}^2 \left[\frac{\partial v_1^{(1)}}{\partial \Lambda} + \frac{1}{2} \sum_{i=1}^{R} \left(\kappa_{2i}^{(1)} \frac{\partial v_{2i\eta}^{(1)}}{\partial \Lambda} + \kappa_{2i+1}^{(1)} \frac{\partial v_{2i\eta+1}^{(1)}}{\partial \Lambda} \right) \right] + \omega_{12}^2 \left[\frac{\partial v_1^{(2)}}{\partial \Lambda} + \frac{1}{2} \sum_{i=1}^{R} \left(\kappa_{2i}^{(2)} \frac{\partial v_{2i\eta}^{(2)}}{\partial \Lambda} + \kappa_{2i+1}^{(2)} \frac{\partial v_{2i\eta+1}^{(2)}}{\partial \Lambda} \right) \right], \tag{A.2}$$

$$\begin{aligned} \frac{\partial S_{2i}^{(1)}}{\partial u_j^{(\ell)}} = & - \left(\frac{\Lambda i}{\eta} \right)^2 \delta_{2i}^{(1)} + 2\zeta_{11}\omega_{11} \left(\frac{\Lambda i}{\eta} \right) \delta_{2i+1}^{(1)} + 2\zeta_{12}\omega_{12} \left(\frac{\Lambda i}{\eta} \right) \delta_{2(i/n)+1}^{(2)} \\ & + \omega_{11}^2 \left[\frac{\partial v_{2i}^{(1)}}{\partial u_j^{(\ell)}} + \kappa_{2\left(\frac{i}{\eta}\right)}^{(1)} \frac{\partial v_1^{(1)}}{\partial u_j^{(\ell)}} \right] + \omega_{12}^2 \left[\frac{\partial v_{2i/n}^{(2)}}{\partial u_j^{(\ell)}} + \kappa_{2\left(\frac{i}{n\eta}\right)}^{(2)} \frac{\partial v_1^{(2)}}{\partial u_j^{(\ell)}} \right] \\ & + \frac{\omega_{11}^2}{2} \sum_{r=1}^{R} \left\{ \kappa_{2r}^{(1)} \left[\frac{\partial v_{2(r\eta-i)}^{(1)}}{\partial u_j^{(\ell)}} + \frac{\partial v_{2(r\eta+i)}^{(1)}}{\partial u_j^{(\ell)}} + \frac{\partial v_{2(i-r\eta)}^{(1)}}{\partial u_j^{(\ell)}} \right] \right. \\ & \left. + \kappa_{2r+1}^{(1)} \left[\frac{\partial v_{2(r\eta-i)+1}^{(1)}}{\partial u_j^{(\ell)}} + \frac{\partial v_{2(r\eta+i)+1}^{(1)}}{\partial u_j^{(\ell)}} - \frac{\partial v_{2(i-r\eta)+1}^{(1)}}{\partial u_j^{(\ell)}} \right] \right\} \\ & + \frac{\omega_{12}^2}{2} \sum_{r=1}^{R} \left\{ \kappa_{2r}^{(2)} \left[\frac{\partial v_{2(r\eta-i/n)}^{(2)}}{\partial u_j^{(\ell)}} + \frac{\partial v_{2(r\eta+i/n)}^{(2)}}{\partial u_j^{(\ell)}} + \frac{\partial v_{2(i/n-r\eta)}^{(2)}}{\partial u_j^{(\ell)}} \right] \right. \\ & \left. + \kappa_{2r+1}^{(2)} \left[\frac{\partial v_{2(r\eta-i/n)+1}^{(2)}}{\partial u_j^{(\ell)}} + \frac{\partial v_{2(r\eta+i/n)+1}^{(2)}}{\partial u_j^{(\ell)}} - \frac{\partial v_{2(i/n-r)+1}^{(2)}}{\partial u_j^{(\ell)}} \right] \right\}, \end{aligned} \tag{A.3}$$

$$\begin{aligned} \frac{\partial S_{2i}^{(1)}}{\partial \Lambda} = & - 2 \left(\frac{i\Lambda}{\eta} \right) u_{2i}^{(1)} + 2\frac{i}{\eta} \zeta_{11}\omega_{11} u_{2i+1}^{(1)} + 2\frac{i}{\eta} \zeta_{12}\omega_{12} u_{2i/n+1}^{(2)} \\ & + \omega_{11}^2 \left[\frac{\partial v_{2i}^{(1)}}{\partial \Lambda} + \kappa_{2i/\eta}^{(1)} \frac{\partial v_1^{(1)}}{\partial \Lambda} \right] + \omega_{12}^2 \left[\frac{\partial v_{2i/n}^{(2)}}{\partial \Lambda} + \kappa_{2i/n\eta}^{(2)} \frac{\partial v_1^{(2)}}{\partial \Lambda} \right] \end{aligned}$$

$$+\frac{\omega_{11}^2}{2}\sum_{r=1}^{R}\left\{\kappa_{2r}^{(1)}\left[\frac{\partial v_{2(r\eta-i)}^{(1)}}{\partial\Lambda}+\frac{\partial v_{2(r\eta+i)}^{(1)}}{\partial\Lambda}+\frac{\partial v_{2(i-r\eta)}^{(1)}}{\partial\Lambda}\right]+\kappa_{2r+1}^{(1)}\left[\frac{\partial v_{2(r\eta-i)+1}^{(1)}}{\partial\Lambda}+\frac{\partial v_{2(r\eta+i)+1}^{(1)}}{\partial\Lambda}-\frac{\partial v_{2(i-r\eta)+1}^{(1)}}{\partial\Lambda}\right]\right\}$$
$$+\frac{\omega_{12}^2}{2}\sum_{r=1}^{R}\left\{\kappa_{2r}^{(2)}\left[\frac{\partial v_{2(r\eta-i/n)}^{(2)}}{\partial\Lambda}+\frac{\partial v_{2(r\eta+i/n)}^{(2)}}{\partial\Lambda}+\frac{\partial v_{2(i/n-r\eta)}^{(2)}}{\partial\Lambda}\right]+\kappa_{2r+1}^{(2)}\left[\frac{\partial v_{2(r\eta-i/n)+1}^{(2)}}{\partial\Lambda}+\frac{\partial v_{2(r\eta+i/n)+1}^{(2)}}{\partial\Lambda}-\frac{\partial v_{2(i/n-r)+1}^{(2)}}{\partial\Lambda}\right]\right\}, \tag{A.4}$$

$$\frac{S_{2i+1}^{(1)}}{\partial u_j^{(\ell)}}=-\left(\frac{\Lambda i}{\eta}\right)^2\delta_{2i+1}^{(1)}-2\zeta_{11}\omega_{11}\left(\frac{\Lambda i}{\eta}\right)\delta_{2i}^{(1)}-2\zeta_{12}\omega_{12}\left(\frac{\Lambda i}{\eta}\right)\delta_{2i/n}^{(2)}$$
$$+\omega_{11}^2\left[\kappa_{2(i/\eta)+1}^{(1)}\frac{\partial v_1^{(1)}}{\partial u_j^{(\ell)}}+\frac{\partial v_{2i+1}^{(1)}}{\partial u_j^{(\ell)}}\right]+\omega_{12}^2\left[\kappa_{(2i/n\eta)+1}^{(2)}\frac{\partial v_1^{(2)}}{\partial u_j^{(\ell)}}+\frac{v_{2(i/n)+1}^{(2)}}{\partial u_j^{(\ell)}}\right]$$
$$+\frac{\omega_{11}^2}{2}\sum_{r=1}^{R}\left\{\kappa_{2r}^{(1)}\left[-\frac{\partial v_{2(r\eta-i)+1}^{(1)}}{\partial u_j^{(\ell)}}+\frac{\partial v_{2(r\eta+i)+1}^{(1)}}{\partial u_j^{(\ell)}}+\frac{\partial v_{2(i-r\eta)+1}^{(1)}}{\partial u_j^{(\ell)}}\right]+\kappa_{2r+1}^{(1)}\left[\frac{\partial v_{2(r\eta-i)}^{(1)}}{\partial u_j^{(\ell)}}-\frac{\partial v_{2(r\eta+i)}^{(1)}}{\partial u_j^{(\ell)}}+\frac{\partial v_{2(i-r\eta)}^{(1)}}{\partial u_j^{(\ell)}}\right]\right\}$$
$$+\frac{\omega_{12}^2}{2}\sum_{r=1}^{R}\left\{\kappa_{2r}^{(2)}\left[-\frac{\partial v_{2(r\eta-i/n)+1}^{(2)}}{\partial u_j^{(\ell)}}+\frac{\partial v_{2(r\eta+i/n)+1}^{(2)}}{\partial u_j^{(\ell)}}+\frac{\partial v_{2(i/n-r\eta)+1}^{(2)}}{\partial u_j^{(\ell)}}\right]+\kappa_{2r+1}^{(2)}\left[\frac{\partial v_{2(r\eta-i/n)}^{(2)}}{\partial u_j^{(\ell)}}-\frac{\partial v_{2(r\eta+i/n)}^{(2)}}{\partial u_j^{(\ell)}}+\frac{\partial v_{2(i/n-r\eta)}^{(2)}}{\partial u_j^{(\ell)}}\right]\right\}, \tag{A.5}$$

$$\frac{\partial S_{2i+1}^{(1)}}{\partial\Lambda}=-2\left(\frac{\Lambda i}{\eta}\right)u_{2i+1}^{(1)}-2\left(\frac{i}{\eta}\right)\zeta_{11}\omega_{11}u_{2i}^{(1)}-2\left(\frac{i}{\eta}\right)\zeta_{12}\omega_{12}u_{2i/n}^{(2)}$$
$$+\omega_{11}^2\left[\kappa_{2(i/\eta)+1}^{(1)}\frac{\partial v_1^{(1)}}{\partial\Lambda}+\frac{\partial v_{2i+1}^{(1)}}{\partial\Lambda}\right]+\omega_{12}^2\left[\kappa_{(2i/n\eta)+1}^{(2)}\frac{\partial v_1^{(2)}}{\partial\Lambda}+\frac{v_{2(i/n)+1}^{(2)}}{\partial\Lambda}\right]$$
$$+\frac{\omega_{11}^2}{2}\sum_{r=1}^{R}\left\{\kappa_{2r}^{(1)}\left[-\frac{\partial v_{2(r\eta-i)+1}^{(1)}}{\partial\Lambda}+\frac{\partial v_{2(r\eta+i)+1}^{(1)}}{\partial\Lambda}+\frac{\partial v_{2(i-r\eta)+1}^{(1)}}{\partial\Lambda}\right]\right.$$

$$+\kappa_{2r+1}^{(1)}\left[\frac{\partial v_{2(r\eta-i)}^{(1)}}{\partial \Lambda}-\frac{\partial v_{2(r\eta+i)}^{(1)}}{\partial \Lambda}+\frac{\partial v_{2(i-r\eta)}^{(1)}}{\partial \Lambda}\right]\Bigg\}$$
$$+\frac{\omega_{12}^2}{2}\sum_{r=1}^{R}\left\{\kappa_{2r}^{(2)}\left[-\frac{\partial v_{2(r\eta-i/n)+1}^{(2)}}{\partial \Lambda}+\frac{\partial v_{2(r\eta+i/n)+1}^{(2)}}{\partial \Lambda}+\frac{\partial v_{2(i/n-r\eta)+1}^{(2)}}{\partial \Lambda}\right]\right.$$
$$\left.+\kappa_{2r+1}^{(2)}\left[\frac{\partial v_{2(r\eta-i/n)}^{(2)}}{\partial \Lambda}-\frac{\partial v_{2(r\eta+i/n)}^{(2)}}{\partial \Lambda}+\frac{\partial v_{2(i/n-r\eta)}^{(2)}}{\partial \Lambda}\right]\right\}, \tag{A.6}$$

$$\frac{\partial S_1^{(2)}}{\partial u_j^{(\ell)}}=\omega_{21}^2\left[\frac{\partial v_1^{(1)}}{\partial u_j^{(\ell)}}+\frac{1}{2}\sum_{r=1}^{R}\left(\kappa_{2r}^{(1)}\frac{\partial v_{2r\eta}^{(1)}}{\partial u_j^{(\ell)}}+\kappa_{2r+1}^{(1)}\frac{\partial v_{2r\eta+1}^{(1)}}{\partial u_j^{(\ell)}}\right)\right]$$
$$+\omega_{22}^2\left[\frac{\partial v_1^{(2)}}{\partial u_j^{(\ell)}}+\frac{1}{2}\sum_{r=1}^{R}\left(\kappa_{2r}^{(2)}\frac{\partial v_{2r\eta}^{(2)}}{\partial u_j^{(\ell)}}+\kappa_{2r+1}^{(2)}\frac{\partial v_{2r\eta+1}^{(2)}}{\partial u_j^{(\ell)}}\right)\right], \tag{A.7}$$

$$\frac{\partial S_1^{(2)}}{\partial \Lambda}=\omega_{21}^2\left[\frac{\partial v_1^{(1)}}{\partial \Lambda}+\frac{1}{2}\sum_{r=1}^{R}\left(\kappa_{2r}^{(1)}\frac{\partial v_{2r\eta}^{(1)}}{\partial \Lambda}+\kappa_{2r+1}^{(1)}\frac{\partial v_{2r\eta+1}^{(1)}}{\partial \Lambda}\right)\right]$$
$$+\omega_{22}^2\left[\frac{\partial v_1^{(2)}}{\partial \Lambda}+\frac{1}{2}\sum_{r=1}^{R}\left(\kappa_{2r}^{(2)}\frac{\partial v_{2r\eta}^{(2)}}{\partial \Lambda}+\kappa_{2r+1}^{(2)}\frac{\partial v_{2r\eta+1}^{(2)}}{\partial \Lambda}\right)\right], \tag{A.8}$$

$$\frac{\partial S_{2i}^{(2)}}{\partial u_j^{(\ell)}}=-\left(\frac{\Lambda r}{\eta}\right)^2\delta_{2i/n}^{(2)}+2\zeta_{21}\omega_{21}\left(\frac{\Lambda r}{\eta}\right)\delta_{2i+1}^{(1)}+2\zeta_{22}\omega_{22}\left(\frac{\Lambda r}{\eta}\right)\delta_{2(i/n)+1}^{(2)}$$
$$+\omega_{21}^2\left[\frac{v_{2i}^{(1)}}{\partial u_j^{(\ell)}}+\frac{v_1^{(1)}}{\partial u_j^{(\ell)}}\kappa_{2i/\eta}^{(1)}\right]+\omega_{22}^2\left[\frac{\partial v_{2i/n}^{(2)}}{\partial u_j^{(\ell)}}+\frac{\partial v_1^{(2)}}{\partial u_j^{(\ell)}}\kappa_{2i/n\eta}^{(2)}\right]$$
$$+\frac{\omega_{21}^2}{2}\sum_{r=1}^{R}\left\{\kappa_{2r}^{(1)}\left[\frac{\partial v_{2(r\eta-i)}^{(1)}}{\partial u_j^{(\ell)}}+\frac{\partial v_{2(r\eta+i)}^{(1)}}{\partial u_j^{(\ell)}}+\frac{\partial v_{2(i-r\eta)}^{(1)}}{\partial u_j^{(\ell)}}\right]\right.$$
$$\left.+\kappa_{2r+1}^{(1)}\left[\frac{\partial v_{2(r\eta-i)+1}^{(1)}}{\partial u_j^{(\ell)}}+\frac{\partial v_{2(r\eta+i)+1}^{(1)}}{\partial u_j^{(\ell)}}-\frac{\partial v_{2(i-r\eta)+1}^{(1)}}{\partial u_j^{(\ell)}}\right]\right\}$$
$$+\frac{\omega_{22}^2}{2}\sum_{r=1}^{R}\left\{\kappa_{2r}^{(2)}\left[\frac{\partial v_{2(r\eta-i/n)}^{(2)}}{\partial u_j^{(\ell)}}+\frac{\partial v_{2(r\eta+i/n)}^{(2)}}{\partial u_j^{(\ell)}}+\frac{\partial v_{2(i/n-r\eta)}^{(2)}}{\partial u_j^{(\ell)}}\right]\right.$$
$$\left.+\kappa_{2r+1}^{(2)}\left[\frac{\partial v_{2(r\eta-i/n)+1}^{(2)}}{\partial u_j^{(\ell)}}+\frac{\partial v_{2(r\eta+i/n)+1}^{(2)}}{\partial u_j^{(\ell)}}-\frac{\partial v_{2(i/n-r\eta)+1}^{(2)}}{\partial u_j^{(\ell)}}\right]\right\}, \tag{A.9}$$

$$\begin{aligned}\frac{\partial S_{2i}^{(2)}}{\partial \Lambda} = & -2\left(\frac{i\Lambda}{\eta}\right)u_{2i/n}^{(2)} + 2\left(\frac{i}{\eta}\right)\zeta_{21}\omega_{21}u_{2i+1}^{(1)} + 2\left(\frac{i}{\eta}\right)\zeta_{22}\omega_{22}u_{2(i/n)+1}^{(2)} \\ & + \omega_{21}^2\left[\frac{v_{2i}^{(1)}}{\partial \Lambda} + \frac{v_1^{(1)}}{\partial \Lambda}\kappa_{2i/\eta}^{(1)}\right] + \omega_{22}^2\left[\frac{\partial v_{2i/n}^{(2)}}{\partial \Lambda} + \frac{\partial v_1^{(2)}}{\partial \Lambda}\kappa_{2i/n\eta}^{(2)}\right] \\ & + \frac{\omega_{21}^2}{2}\sum_{r=1}^{R}\left\{\kappa_{2r}^{(1)}\left[\frac{\partial v_{2(r\eta-i)}^{(1)}}{\partial \Lambda} + \frac{\partial v_{2(r\eta+i)}^{(1)}}{\partial \Lambda} + \frac{\partial v_{2(i-r\eta)}^{(1)}}{\partial \Lambda}\right]\right. \\ & \left. + \kappa_{2r+1}^{(1)}\left[\frac{\partial v_{2(r\eta-i)+1}^{(1)}}{\partial \Lambda} + \frac{\partial v_{2(r\eta+i)+1}^{(1)}}{\partial \Lambda} - \frac{\partial v_{2(i-r\eta)+1}^{(1)}}{\partial \Lambda}\right]\right\} \\ & + \frac{\omega_{22}^2}{2}\sum_{r=1}^{R}\left\{\kappa_{2r}^{(2)}\left[\frac{\partial v_{2(r\eta-i/n)}^{(2)}}{\partial \Lambda} + \frac{\partial v_{2(r\eta+i/n)}^{(2)}}{\partial \Lambda} + \frac{\partial v_{2(i/n-r\eta)}^{(2)}}{\partial \Lambda}\right]\right. \\ & \left. + \kappa_{2r+1}^{(2)}\left[\frac{\partial v_{2(r\eta-i/n)+1}^{(2)}}{\partial \Lambda} + \frac{\partial v_{2(r\eta+i/n)+1}^{(2)}}{\partial \Lambda} - \frac{\partial v_{2(i/n-r\eta)+1}^{(2)}}{\partial \Lambda}\right]\right\}, \end{aligned} \tag{A.10}$$

$$\begin{aligned}\frac{\partial S_{2i+1}^{(2)}}{\partial u_j^{(\ell)}} = & -\left(\frac{r\Lambda}{\eta}\right)^2\delta_{2(i/n)+1}^{(2)} - 2\zeta_{21}\omega_{21}\left(\frac{\Lambda r}{\eta}\right)\delta_{2i}^{(1)} - 2\zeta_{22}\omega_{22}\left(\frac{\Lambda r}{\eta}\right)\delta_{2i/n}^{(2)} \\ & + \omega_{21}^2\left[\frac{\partial v_1^{(1)}}{\partial u_j^{(\ell)}}\kappa_{2(i/\eta)+1}^{(1)} + \frac{\partial v_{2i+1}^{(1)}}{\partial u_j^{(\ell)}}\right] + \omega_{22}^2\left[\frac{\partial v_1^{(2)}}{\partial u_j^{(\ell)}}\kappa_{2(i/n\eta)+1}^{(2)} + \frac{\partial v_{2(i/n)+1}^{(2)}}{\partial u_j^{(\ell)}}\right] \\ & + \frac{\omega_{21}^2}{2}\sum_{r=1}^{R}\left\{\kappa_{2r}^{(1)}\left[-\frac{\partial v_{2(r\eta-i)+1}^{(1)}}{\partial u_j^{(\ell)}} + \frac{\partial v_{2(r\eta+i)+1}^{(1)}}{\partial u_j^{(\ell)}} + \frac{\partial v_{2(i-r\eta)+1}^{(1)}}{\partial u_j^{(\ell)}}\right]\right. \\ & \left. + \kappa_{2r+1}^{(1)}\left[\frac{\partial v_{2(r\eta-i)}^{(1)}}{\partial u_j^{(\ell)}} - \frac{\partial v_{2(r\eta+i)}^{(1)}}{\partial u_j^{(\ell)}} + \frac{\partial v_{2(i-r\eta)}^{(1)}}{\partial u_j^{(\ell)}}\right]\right\} \\ & + \frac{\omega_{22}^2}{2}\sum_{r=1}^{R}\left\{\kappa_{2r}^{(2)}\left[-\frac{\partial v_{2(r\eta-i/n)+1}^{(2)}}{\partial u_j^{(\ell)}} + \frac{\partial v_{2(r\eta+i/n)+1}^{(2)}}{\partial u_j^{(\ell)}} + \frac{\partial v_{2(i/n-r\eta)+1}^{(2)}}{\partial u_j^{(\ell)}}\right]\right. \\ & \left. + \kappa_{2r+1}^{(2)}\left[\frac{\partial v_{2(r\eta-i/n)}^{(2)}}{\partial u_j^{(\ell)}} - \frac{\partial v_{2(r\eta+i/n)}^{(2)}}{\partial u_j^{(\ell)}} + \frac{\partial v_{2(i/n-r\eta)}^{(2)}}{\partial u_j^{(\ell)}}\right]\right\}, \end{aligned} \tag{A.11}$$

$$\begin{aligned}\frac{\partial S_{2i+1}^{(2)}}{\partial \Lambda} = & -2\left(\frac{i\Lambda}{\eta}\right)u_{2(i/n)+1}^{(2)} - 2\left(\frac{i}{\eta}\right)\zeta_{21}\omega_{21}u_{2i}^{(1)} - 2\left(\frac{i}{\eta}\right)\zeta_{22}\omega_{22}u_{2i/n}^{(2)} \\ & + \omega_{21}^2\left[\frac{\partial v_1^{(1)}}{\partial \Lambda}\kappa_{2(i/\eta)+1}^{(1)} + \frac{\partial v_{2i+1}^{(1)}}{\partial \Lambda}\right] + \omega_{22}^2\left[\frac{\partial v_1^{(2)}}{\partial \Lambda}\kappa_{2(i/n\eta)+1}^{(2)} + \frac{\partial v_{2(i/n)+1}^{(2)}}{\partial \Lambda}\right] \end{aligned}$$

$$+\frac{\omega_{21}^2}{2}\sum_{r=1}^{R}\left\{\kappa_{2r}^{(1)}\left[-\frac{\partial v_{2(r\eta-i)+1}^{(1)}}{\partial\Lambda}+\frac{\partial v_{2(r\eta+i)+1}^{(1)}}{\partial\Lambda}+\frac{\partial v_{2(i-r\eta)+1}^{(1)}}{\partial\Lambda}\right]\right.$$
$$\left.+\kappa_{2r+1}^{(1)}\left[\frac{\partial v_{2(r\eta-i)}^{(1)}}{\partial\Lambda}-\frac{\partial v_{2(r\eta+i)}^{(1)}}{\partial\Lambda}+\frac{\partial v_{2(i-r\eta)}^{(1)}}{\partial\Lambda}\right]\right\}$$
$$+\frac{\omega_{22}^2}{2}\sum_{r=1}^{R}\left\{\kappa_{2r}^{(2)}\left[-\frac{\partial v_{2(r\eta-i/n)+1}^{(2)}}{\partial\Lambda}+\frac{\partial v_{2(r\eta+i/n)+1}^{(2)}}{\partial\Lambda}+\frac{\partial v_{2(i/n-r\eta)+1}^{(2)}}{\partial\Lambda}\right]\right.$$
$$\left.+\kappa_{2r+1}^{(2)}\left[\frac{\partial v_{2(r\eta-i/n)}^{(2)}}{\partial\Lambda}-\frac{\partial v_{2(r\eta+i/n)}^{(2)}}{\partial\Lambda}+\frac{\partial v_{2(i/n-r\eta)}^{(2)}}{\partial\Lambda}\right]\right\}, \tag{A.12}$$

$$\frac{\partial S_{4R+3}}{\partial u_j^{(\ell)}}=1, \tag{A.13}$$

where $\delta_i^{(k)}$, $k=1,2$, is the Kronecker δ defined as

$$\delta_i^{(k)}=\begin{cases}1, & i=j \text{ and } k=\ell,\\ 0, & \text{elsewhere.}\end{cases} \tag{A.14}$$

The partial derivatives $\partial v_i^{(k)}/\partial u_j^{(\ell)}$ $(k,\ell=1,2)$ are given as

$$\frac{\partial v_i^{(k)}}{\partial u_j^{(\ell)}}=0, \quad k\neq\ell, \quad j\neq 2R+2, \tag{A.15}$$

$$\frac{\partial v_1^{(1)}}{\partial u_1^{(1)}}=\frac{1}{Q}\sum_{q=0}^{Q-1}\frac{\partial g_{1q}}{\partial u_1^{(1)}}=\frac{1}{Q}\sum_{q=0}^{Q-1}\phi_{1q}, \tag{A.16}$$

$$\frac{\partial v_1^{(1)}}{\partial u_{2j}^{(1)}}=\frac{1}{Q}\sum_{q=0}^{Q-1}\frac{\partial g_{1q}}{\partial u_{2j}^{(1)}}=\frac{1}{Q}\sum_{q=0}^{Q-1}\phi_{1q}\cos\left(\frac{2\pi qj}{Q}\right), \quad j\in[1,R], \tag{A.17}$$

$$\frac{\partial v_1^{(1)}}{\partial u_{2j+1}^{(1)}}=\frac{1}{Q}\sum_{q=0}^{Q-1}\frac{\partial g_{1q}}{\partial u_{2j+1}^{(1)}}=\frac{1}{Q}\sum_{q=0}^{Q-1}\phi_{1q}\sin\left(\frac{2\pi qj}{Q}\right), \quad j\in[1,R], \tag{A.18}$$

$$\frac{\partial v_1^{(1)}}{\partial\Lambda}=\frac{1}{Q}\sum_{q=0}^{Q-1}\frac{\partial g_{1q}}{\partial\Lambda}, \tag{A.19}$$

$$\frac{\partial v_{2i}^{(1)}}{\partial u_1^{(1)}}=\frac{2}{Q}\sum_{q=0}^{Q-1}\frac{\partial g_{1q}}{\partial u_1^{(1)}}\cos\left(\frac{2\pi qi}{Q}\right)=\frac{2}{Q}\sum_{q=0}^{Q-1}\phi_{1q}\cos\left(\frac{2\pi qi}{Q}\right), \quad i\in[1,R], \tag{A.20}$$

$$\frac{\partial v_{2i}^{(1)}}{\partial u_{2j}^{(1)}}=\frac{2}{Q}\sum_{q=0}^{Q-1}\frac{\partial g_{1q}}{\partial u_{2j}^{(1)}}\cos\left(\frac{2\pi qi}{Q}\right)=\frac{2}{Q}\sum_{q=0}^{q-1}\phi_{1q}\cos\left(\frac{2\pi qi}{Q}\right)\cos\left(\frac{2\pi qj}{Q}\right), \quad i,j\in[1,R], \tag{A.21}$$

$$\frac{\partial v_{2i}^{(1)}}{\partial u_{2j+1}^{(1)}} = \frac{2}{Q}\sum_{q=0}^{Q-1}\frac{\partial g_{1q}}{\partial u_{2j+1}^{(1)}}\cos\left(\frac{2\pi qi}{Q}\right) = \frac{2}{Q}\sum_{q=0}^{Q-1}\phi_{1q}\cos\left(\frac{2\pi qi}{Q}\right)\sin\left(\frac{2\pi qj}{Q}\right), \quad i,j\in[1,R], \tag{A.22}$$

$$\frac{\partial v_{2i}^{(1)}}{\partial \Lambda} = \frac{2}{Q}\sum_{q=0}^{Q-1}\left\{\frac{\partial g_{1q}}{\partial \Lambda}\cos\left(\frac{2\pi qi}{Q}\right) - g_{1q}\left(\frac{2\pi iq}{\Lambda Q}\right)\sin\left(\frac{2\pi iq}{Q}\right)\right\}, \quad i\in[1,R], \tag{A.23}$$

$$\frac{\partial v_{2i+1}^{(1)}}{\partial u_{1}^{(1)}} = \frac{2}{Q}\sum_{q=0}^{Q-1}\frac{\partial g_{1q}}{\partial u_{1}^{(1)}}\sin\left(\frac{2\pi qi}{Q}\right) = \frac{2}{Q}\sum_{q=0}^{Q-1}\phi_{1q}\sin\left(\frac{2\pi qi}{Q}\right), \quad i\in[1,R], \tag{A.24}$$

$$\frac{\partial v_{2i+1}^{(1)}}{\partial u_{2j}^{(1)}} = \frac{2}{Q}\sum_{q=0}^{Q-1}\frac{\partial g_{1q}}{\partial u_{2j}^{(1)}}\sin\left(\frac{2\pi qi}{Q}\right) = \frac{2}{Q}\sum_{q=0}^{Q-1}\phi_{1q}\sin\left(\frac{2\pi qi}{Q}\right)\cos\left(\frac{2\pi qj}{Q}\right), \quad i,j\in[1,R], \tag{A.25}$$

$$\frac{\partial v_{2i+1}^{(1)}}{\partial u_{2j+1}^{(1)}} = \frac{2}{Q}\sum_{q=0}^{Q-1}\frac{\partial g_{1q}}{\partial u_{2j+1}^{(1)}}\sin\left(\frac{2\pi qi}{Q}\right) = \frac{2}{Q}\sum_{q=0}^{Q-1}\phi_{1q}\sin\left(\frac{2\pi qi}{Q}\right)\sin\left(\frac{2\pi qj}{Q}\right), \quad i,j\in[1,R], \tag{A.26}$$

$$\frac{\partial v_{2i+1}^{(1)}}{\partial \Lambda} = \frac{2}{Q}\sum_{q=0}^{Q-1}\left\{\frac{\partial g_{1q}}{\partial \Lambda}\sin\left(\frac{2\pi qi}{Q}\right) + g_{1q}\left(\frac{2\pi qj}{\Lambda Q}\right)\cos\left(\frac{2\pi qj}{Q}\right)\right\}, \quad i\in[1,R], \tag{A.27}$$

$$\frac{\partial v_{1}^{(2)}}{\partial u_{1}^{(2)}} = \frac{1}{Q}\sum_{q=0}^{Q-1}\frac{\partial g_{2q}}{\partial u_{1}^{(2)}} = \frac{1}{Q}\sum_{q=0}^{Q-1}\phi_{2q}, \tag{A.28}$$

$$\frac{\partial v_{1}^{(2)}}{\partial u_{2j}^{(2)}} = \frac{1}{Q}\sum_{q=0}^{Q-1}\frac{\partial g_{2q}}{\partial u_{2j}^{(2)}} = \frac{1}{Q}\sum_{q=0}^{Q-1}\phi_{2q}\cos\left(\frac{2\pi nqj}{Q}\right), \quad j\in[1,R], \tag{A.29}$$

$$\frac{\partial v_{1}^{(2)}}{\partial u_{2j+1}^{(2)}} = \frac{1}{Q}\sum_{q=0}^{Q-1}\frac{\partial g_{2q}}{\partial u_{2j+1}^{(2)}} = \frac{1}{Q}\sum_{q=0}^{Q-1}\phi_{2q}\sin\left(\frac{2\pi nqj}{Q}\right), \quad i\in[1,R], \tag{A.30}$$

$$\frac{\partial v_{1}^{(2)}}{\partial \Lambda} = \frac{1}{Q}\sum_{q=0}^{Q-1}\frac{\partial g_{2q}}{\partial \Lambda}, \tag{A.31}$$

$$\frac{\partial v_{2i}^{(2)}}{\partial u_{1}^{(2)}} = \frac{2}{Q}\sum_{q=0}^{Q-1}\frac{\partial g_{2q}}{\partial u_{1}^{(2)}}\cos\left(\frac{2\pi nqi}{Q}\right) = \frac{2}{Q}\sum_{q=0}^{Q-1}\phi_{2q}\cos\left(\frac{2\pi nqi}{Q}\right), \quad i\in[1,R], \tag{A.32}$$

$$\frac{\partial v_{2i}^{(2)}}{\partial u_{2j}^{(2)}} = \frac{2}{Q}\sum_{q=0}^{Q-1}\frac{\partial g_{2q}}{\partial u_{2j}^{(2)}}\cos\left(\frac{2\pi nqi}{Q}\right) = \frac{2}{Q}\sum_{q=0}^{Q-1}\phi_{2q}\cos\left(\frac{2\pi nqi}{Q}\right)\cos\left(\frac{2\pi nqj}{Q}\right), \quad i,j\in[1,R], \tag{A.33}$$

$$\frac{\partial v_{2i}^{(2)}}{\partial u_{2j+1}^{(2)}} = \frac{2}{Q}\sum_{q=0}^{Q-1}\frac{\partial g_{2q}}{\partial u_{2j+1}^{(2)}}\cos\left(\frac{2\pi nqi}{Q}\right) = \frac{2}{Q}\sum_{q=0}^{Q-1}\phi_{2q}\cos\left(\frac{2\pi nqi}{Q}\right)\sin\left(\frac{2\pi nqj}{Q}\right), \quad i,j\in[1,R], \tag{A.34}$$

$$\frac{\partial v_{2i}^{(2)}}{\partial \Lambda} = \frac{2}{Q}\sum_{q=0}^{Q-1}\left\{\frac{\partial g_{2q}}{\partial \Lambda}\cos\left(\frac{2\pi nqi}{Q}\right) - g_{2q}\left(\frac{2\pi nqi}{\Lambda Q}\right)\sin\left(\frac{2\pi nqj}{Q}\right)\right\}, \quad i\in[1,R], \tag{A.35}$$

$$\frac{\partial v_{2i+1}^{(2)}}{\partial u_1^{(2)}} = \frac{2}{Q}\sum_{q=0}^{Q-1}\frac{\partial g_{2q}}{\partial u_1^{(2)}}\sin\left(\frac{2\pi nqi}{Q}\right) = \frac{2}{Q}\sum_{q=0}^{Q-1}\phi_{2q}\sin\left(\frac{2\pi nqi}{Q}\right), \quad i\in[1,R], \tag{A.36}$$

$$\frac{\partial v_{2i+1}^{(2)}}{\partial u_{2j}^{(2)}} = \frac{2}{Q}\sum_{q=0}^{Q-1}\frac{\partial g_{2q}}{\partial u_{2j}^{(2)}}\sin\left(\frac{2\pi nqi}{Q}\right) = \frac{2}{Q}\sum_{q=0}^{Q-1}\phi_{2q}\sin\left(\frac{2\pi nqi}{Q}\right)\cos\left(\frac{2\pi nqj}{Q}\right), \quad i,j\in[1,R], \tag{A.37}$$

$$\frac{\partial v_{2i+1}^{(2)}}{\partial u_{2j+1}^{(2)}} = \frac{2}{Q}\sum_{q=0}^{Q-1}\frac{\partial g_{2q}}{\partial u_{2j+1}^{(2)}}\sin\left(\frac{2\pi nqi}{Q}\right) = \frac{2}{Q}\sum_{q=0}^{Q-1}\phi_{2q}\sin\left(\frac{2\pi nqi}{Q}\right)\sin\left(\frac{2\pi nqj}{Q}\right), \quad i,j\in[1,R], \tag{A.38}$$

$$\frac{\partial v_{2i+1}^{(2)}}{\partial \Lambda} = \frac{2}{Q}\sum_{q=0}^{Q-1}\left\{\frac{\partial g_{2q}}{\partial \Lambda}\sin\left(\frac{2\pi nqi}{Q}\right) + g_{2q}\left(\frac{2\pi nqi}{\Lambda Q}\right)\cos\left(\frac{2\pi nqi}{Q}\right)\right\}, \quad i\in[1,R]. \tag{A.39}$$

Here ϕ_{1q} and ϕ_{2q} are discrete separation functions [4] given by

$$\phi_{iq} = \begin{cases} 1, & |p_i(t)| > b_i, \\ 0, & |p_i(t)| \leqslant b_i, \end{cases} \quad i = 1,2, \tag{A.40}$$

and

$$\frac{\partial g_{1q}}{\partial \Lambda} = \begin{cases} \sum_{r=1}^{R}\left[-\left(\frac{2\pi rq}{\Lambda Q}\right)u_{2r}^{(1)}\sin\left(\frac{2\pi rq}{Q}\right) + \left(\frac{2\pi rq}{\Lambda Q}\right)u_{2r+1}^{(1)}\cos\left(\frac{2\pi rq}{Q}\right)\right], & |p_{1q}| > b_1, \\ 0, & |p_{1q}| < b_1, \end{cases} \tag{A.41}$$

$$\frac{\partial g_{2q}}{\partial \Lambda} = \begin{cases} \sum_{r=1}^{R}\left[-\left(\frac{2\pi rq}{\Lambda Q}\right)u_{2r}^{(2)}\sin\left(\frac{2\pi rq}{Q}\right) + \left(\frac{2\pi rq}{\Lambda Q}\right)u_{2r+1}^{(2)}\cos\left(\frac{2\pi rq}{Q}\right)\right], & |p_{2q}| > b_2, \\ 0, & |p_{2q}| < b_2. \end{cases} \tag{A.42}$$

Appendix B. Nomenclature

b	half of clearance (backlash)
c	damping coefficient
e	gear motion transmission error
f	external force
g	discontinuous displacement function
HBM	harmonic balance method
I	polar mass moment of inertia
k	gear mesh stiffness
m	mass
NI	numerical integration
p	relative gear mesh displacement

Q number of discrete time points
q discrete time interval
R number of harmonic components considered in the solution
r radius
r.m.s. root mean square
$\mathbf{S}$ matrix form of non-linear algebraic equation set
T torque
T fundamental period
t time
u harmonic amplitude of response
$\mathbf{U}$ displacement vector
v describing function
Z number of gear teeth
δ Kronecker delta
η sub-harmonic index
Λ dimensionless frequency
κ dimensionless mesh stiffness
θ rotational displacement
ρ number
ω characteristic frequency
Ω nominal rigid body angular velocity
ζ damping ratio

Subscripts

a alternating component
c characteristic quantity
eq equivalent
i gear index
m mean component
ni ith natural mode

Superscripts

ℓ gear mesh index ($\ell = 1, 2$)
r.m.s. root-mean-square value
T matrix transpose

References

[1] H. Vinayak, R. Singh, C. Padmanabhan, Linear dynamic analysis of multi-mesh transmissions containing external rigid gears, *Journal of Sound and Vibration* 185 (1995) 1–32.
[2] S.H. Choi, J. Glienicke, D.C. Han, K. Urlichs, Dynamic gear load due to coupled lateral, torsional and axial vibrations in a helical geared system, *Journal of Vibration and Acoustics* 121 (1999) 141–148.

[3] T.C. Lim, J. Li, Dynamic analysis of multi-mesh counter-shaft transmission, *Journal of Sound and Vibration* 219 (1999) 905–918.
[4] A. Kahraman, Effect of axial vibrations on the dynamics of a helical gear pair, *Journal of Vibration and Acoustics* 115 (1993) 33–39.
[5] A. Kahraman, Dynamic analysis of a multi-mesh helical gear train, *Journal of Mechanical Design* 116 (1994) 706–712.
[6] H. Iida, A. Tamura, K. Kikuchi, H. Agata, Coupled torsional-flexural vibration of a shaft in a geared system of rotors (1st Report), *Bulletin of the JSME* 23 (1980) 2111–2117.
[7] H. Iida, A. Tamura, M. Oonishi, Coupled torsional-flexural vibration of a shaft in a geared system (3rd Report), *Bulletin of the JSME* 28 (1985) 2694–2698.
[8] H. Iida, A. Tamura, H. Yamamoto, Dynamic characteristics of a gear train system with softly supported shafts, *Bulletin of the JSME* 29 (1986) 1811–1816.
[9] S.V. Neriya, R.B. Bhat, T.S. Sankar, Effect of coupled torsional-flexural vibration of a geared shaft system on the dynamic tooth load, *The Shock and Vibration Bulletin* 54 (1984) 67–75.
[10] S.V. Neriya, R.B. Bhat, T.S. Sankar, Dynamic tooth load and response of a torsion–flexure coupled geared shaft system due to internal excitations, in: *Proceedings of the ASME 21th Biennial Mechanisms Conference on Cams, Gears, Robots and Machine Design*, Chicago, IL, 1990.
[11] T. Iwatsubo, S. Arii, R. Kawai, Coupled lateral-torsional vibration of rotor system trained by gears, *Bulletin of the JSME* 27 (1984) 271–277.
[12] K. Umezawa, T. Ajima, H. Houjoh, Vibration of three axis gear system, *Bulletin of JSME* 29 (1986) 950–957.
[13] M. Kubur, A. Kahraman, D. Zini, K. Kienzle, Dynamic analysis of a multi-shaft helical gear transmission by finite elements: model and experiment, *Journal of Vibration and Acoustics* 126 (2004) 398–406.
[14] A. Kahraman, G.W. Blankenship, Experiments on nonlinear dynamic behavior of an oscillator with clearance and periodically time-varying parameters, *Journal of Applied Mechanics* 64 (1997) 217–226.
[15] G.W. Blankenship, A. Kahraman, Steady state forced response of a mechanical oscillator with combined parametric excitation and clearance type non-linearity, *Journal of Sound and Vibration* 185 (1994) 734–765.
[16] A. Kahraman, G.W. Blankenship, Interactions between commensurate parametric and forcing excitations in a system with clearance, *Journal of Sound and Vibration* 194 (1996) 317–335.
[17] A. Kahraman, G.W. Blankenship, Effect of involute contact ratio on spur gear dynamics, *Journal of Mechanical Design* 121 (1999) 112–118.
[18] M. Benton, A. Seireg, Simulation of responses and instability conditions in a pinion-gear system, *Journal of Mechanical Design* 100 (1978) 26–32.
[19] M. Benton, A. Seireg, Factors influencing instability and resonances in geared systems, *Journal of Mechanical Design* 103 (1981) 372–378.
[20] W. Mollers, Parametererregte Schwingungen in einstufigen Zylinderradgetrieben, Ph.D. Dissertation, Rheinisch-Westfalischen Technischen Hochschule, Aachen, 1982.
[21] T. Nakada, M. Utagawa, The dynamic loads on gears caused by the varying elasticity of the mating teeth, in: *Proceedings of the Sixth Japan National Congress for Applied Mechanics*, 1956, pp. 493–497.
[22] J. Lin, R.G. Parker, Mesh stiffness vibration instabilities in two-stage gear systems, *Journal of Vibration and Acoustics* 124 (2002) 68–76.
[23] R.W. Gregory, S.L. Harris, R.G. Monro, Dynamic behavior of spur gears, *Proceedings of the Institution of Mechanical Engineers* 178 (1963–1964) 207–226.
[24] K. Umezawa, T. Ajima, H. Houjoh, Vibration of three axes gear systems, *Bulletin of JSME* 29 (1986) 950–957.
[25] A. Kahraman, R. Singh, Interactions between time-varying mesh stiffness and clearance non-linearities in a geared system, *Journal of Sound and Vibration* 146 (1991) 135–156.
[26] A. Al-shyyab, A. Kahraman, Nonlinear dynamic analysis of a multi-mesh gear train using multi-term harmonic balance method: period-one motions, *Journal of Sound and Vibration*, in press; doi:10.1016/j.jsv.2004.06.010.